






# Impact of calcium and copper co-doping on the oxygen transport of layered nickelates: a case study of $\text{Pr}_{1.6}\text{Ca}_{0.4}\text{Ni}_{1-y}\text{Cu}_y\text{O}_{4+\delta}$ and a comparative analysis

Vladislav Sadykov <sup>a</sup> , Nikita Ereemeev <sup>a\*</sup> , Ekaterina Sadovskaya <sup>a</sup>,  
Tatiana Zhulanova <sup>bc</sup> , Sergey Pikalov <sup>d</sup> , Yulia Fedorova <sup>a</sup>,  
Elena Pikalova <sup>bc</sup> 

**a:** Federal Research Center Boreskov Institute of Catalysis SB RAS, Novosibirsk 630090, Russia  
**b:** Institute of High-Temperature Electrochemistry UB RAS, Ekaterinburg 620137, Russia  
**c:** Graduate School of Economics and Management, Ural Federal University, Ekaterinburg 620002, Russia  
**d:** Institute of Metallurgy UB RAS, Ekaterinburg, 620137, Russia  
\* Corresponding author: [yereemeev21@catalysis.ru](mailto:yereemeev21@catalysis.ru)



This paper belongs to a Regular Issue.

## Abstract

This study aims at investigating oxygen content and diffusion in the  $\text{Pr}_{1.6}\text{Ca}_{0.4}\text{Ni}_{1-y}\text{Cu}_y\text{O}_{4+\delta}$  ( $y = 0.0-0.4$ ) series. Single-phased materials were obtained via nitrate combustion using glycerol as a fuel. The materials exhibit an orthorhombic structure, which correlates well with the absolute oxygen content in the samples in the range of 4.15–3.97. The oxygen mobility in the samples was investigated by a temperature-programmed isotope exchange of oxygen (TPIE) with  $\text{C}^{18}\text{O}_2$  in a flow reactor. The obtained curves, comprising few extrema, were fitted using a mathematical model that includes two or three distinct oxygen forms, each characterized by a specific diffusion coefficient value. The oxygen tracer diffusion coefficient values and the contribution of fast oxygen forms tend to decrease with increasing Cu content (except for  $\text{Pr}_{1.6}\text{Ca}_{0.4}\text{Ni}_{0.8}\text{Cu}_{0.2}\text{O}_{4+\delta}$ ), which can be explained by the variation of highly mobile interstitial oxygen content since the effective activation energy values remains the same within the calculation error. Comparative analysis shows that this behavior is similar to the trends observed and discussed for Ca- and Cu-doped La and Nd nickelates. Nevertheless, the highest  $D^*$  value for  $\text{O}_{\text{fast}}$  was demonstrated for the  $\text{Pr}_{1.6}\text{Ca}_{0.4}\text{Ni}_{0.8}\text{Cu}_{0.2}\text{O}_{4+\delta}$  sample ( $9.4 \cdot 10^{-8} \text{ cm}^2/\text{s}$  at  $700 \text{ }^\circ\text{C}$ ), which correlates well with superior electrochemical properties of the electrodes on its basis.

## Keywords

solid oxide fuel cells  
solid oxide electrolyzers  
layered nickelates  
oxygen transport  
isotope exchange of oxygen

Received: 19.09.24  
Revised: 17.10.24  
Accepted: 24.10.24  
Available online: 06.11.24

## Key findings

- Oxygen tracer diffusion coefficient values tend to decrease with increasing Cu content.
- There is a nonuniformity in oxygen mobility expressed in 2 or 3 form of oxygen.
- The trends in the oxygen transport properties are similar to those for the Ca- and Cu-doped La and Nd nickelates.

© 2024, the Authors. This article is published in open access under the terms and conditions of the Creative Commons Attribution (CC BY) license (<http://creativecommons.org/licenses/by/4.0/>).



## 1. Introduction

The  $\text{Ln}_2\text{NiO}_{4+\delta}$  ( $\text{Ln} = \text{La}, \text{Pr}, \text{Nd}$ ) phases, as representatives of the first-order Ruddlesden–Popper (RP) phases, have been extensively studied in the last two decades as air electrodes for solid oxide fuel cells (SOFCs) [1–8], solid oxide electrolysis cells (SOECs) [9–13], oxygen separation membranes [14–19], and catalysts for hydrocarbon fuel

conversion into syngas [20, 21] and other reactions [22, 23]. The variety of applications has been attributed to several factors, including a moderate thermal expansion coefficient, stability under operating conditions, high catalytic and electrocatalytic activity in the respective reactions, low polarization resistance, and high oxygen permeability. These properties have been provided by the layered structure, high mixed ionic ( $\text{O}^{2-}$  and occasionally  $\text{H}^+$ )-electronic

conductivity, and ability to exsolve metal nanoparticles under reducing conditions [20, 23].

The high oxygen ionic conductivity characteristics of RP phases are due to the cooperative mechanism of oxygen migration via interstitialcy movement involving both regular and interstitial oxygen [24–27]. The interstitial oxygen of the rock salt layer is known to be highly mobile and capable of accumulating to a high extent. This mechanism results in high oxygen self-diffusion coefficient values (up to  $\sim 10^{-8}$ – $10^{-7}$  cm<sup>2</sup>/s at 700 °C [28,29]), which are attractive for electrochemical and catalytic applications [1,7,14]. At the same time, the total conductivity of RP phases is moderate and exhibits a bell-shaped dependence on temperature, reaching a maximum in the 400–550 °C range, followed by a decrease at higher temperatures due to the reduction in charge carriers caused by oxygen release from the layered structure [1, 30]. It is essential to enhance the maximal conductivity values, which are typically less than 10<sup>2</sup> S cm<sup>-1</sup> for undoped Ln<sub>2</sub>NiO<sub>4+δ</sub>, with the objective of facilitating more efficient electrochemical and catalytic applications. A number of studies demonstrated that doping Ln-site with alkaline earth metals (AEMs) enhances the total conductivity, particularly when Ca is employed as a dopant (in comparison with oxides with equal AEM dopant concentrations) [31–33]. Nevertheless, AEM doping resulted in a reduction in oxygen mobility, attributed to a decrease in the interstitial oxygen content and steric hindrances for the cooperative mechanism [29, 34–36]. Additionally, AEM doping was shown to increase the thermal expansion coefficient [1, 7].

Doping at the Ni-site is another approach to modify the functional properties of RP phases. Doping with cations such as Mg, Mn, Fe, Co, Cu, Ga or their combinations can result in modifying the thermal and chemical expansion behavior of the oxides and compensating for the negative effects or enhancing the positive influence of Ln-site doping [37–43]. Ni-site doping can either increase or decrease the oxygen mobility and may sometimes have an even more pronounced influence than Ln-site doping [39, 44–48].

Typically, the doping of Ln<sub>2</sub>NiO<sub>4+δ</sub> at the Ni-site with Cu results in a decrease in total conductivity; however, at certain concentrations, it can improve the thermomechanical compatibility of RP phases with solid-state electrolytes and increase the electrochemical activity of the electrodes [40, 45, 49–51]. Nevertheless, the information on the effects of doping with Cu on the oxygen transport properties is contradictory. Doping Ln nickelates with Cu resulted in either an increase or a decrease in the oxygen mobility due to the effects of the energy barrier for interstitial oxygen migration, interstitial oxygen content, grain growth features, changes in the (Ni,Cu)–O bond length, and other factors [46, 52–55].

This work continues the series of systematic studies concerning the structure, functional properties and electrochemical applications of Ln<sub>2</sub>NiO<sub>4+δ</sub> (Ln = Nd, La, Pr), double doped with Ca and Cu at the Ln and Ni sites,

respectively [40, 44, 47, 56–58]. The novelty of this work is a comprehensive study of oxygen transport characteristics of the Pr<sub>1.6</sub>Ca<sub>0.4</sub>Ni<sub>1-y</sub>Cu<sub>y</sub>O<sub>4+δ</sub> series, which is performed for the first time. This paper also provides a summary of the structural properties, oxygen content and other characteristics of the materials of the Ln<sub>1-x</sub>Ca<sub>x</sub>Ni<sub>1-y</sub>Cu<sub>y</sub>O<sub>4+δ</sub> series, as well as a comparative analysis of their functional properties and electrochemical characteristics. It was demonstrated that Pr-based materials exhibit superior electrochemical performance in this series. For example, the polarization resistance ( $R_p$ ) of the Pr<sub>1.6</sub>Ca<sub>0.4</sub>Ni<sub>0.8</sub>Cu<sub>0.2</sub>O<sub>4+δ</sub> electrode was found to be in the range of 0.19–0.27 Ω cm<sup>2</sup> (at 700 °C) depending on the electrolyte substrate (Ce<sub>0.8</sub>Sm<sub>0.2</sub>O<sub>2-δ</sub>, doped BaCe(Zr)O<sub>3-δ</sub>) [57] compared with those obtained for Nd-based (2.73–4.79 Ω cm<sup>2</sup> at 700 °C [47] and La-based (1.95 Ω cm<sup>2</sup> at 700 °C [40]) electrodes. Given that RP phases are mixed ion- and electron-conducting (MIEC) materials and that their electrochemical properties are strongly dependent on their oxygen transport properties [59], this study aims to investigate the oxygen content and diffusion in the Pr<sub>1.6</sub>Ca<sub>0.4</sub>Ni<sub>1-y</sub>Cu<sub>y</sub>O<sub>4+δ</sub> ( $y = 0.0$ – $0.4$ ) series. The data obtained were employed to determine the correlations between the oxygen diffusion kinetics and electrochemical properties, as well as to compare them with undoped, Ca-doped and Ca/Cu-doped Ln<sub>2</sub>NiO<sub>4+δ</sub>.

## 2. Materials and methods

Materials of the Pr<sub>1.6</sub>Ca<sub>0.4</sub>Ni<sub>1-y</sub>Cu<sub>y</sub>O<sub>4+δ</sub> ( $y = 0.0$ – $0.4$ , PCNO, PCNCO1–PCNCO4) series were synthesized by nitrate combustion using glycerol as a fuel, with high purity reagents, namely, Pr<sub>6</sub>O<sub>11</sub> (98% purity), CaCO<sub>3</sub> ( $\geq 97\%$  purity), Ni(CH<sub>3</sub>COO)<sub>2</sub>·4H<sub>2</sub>O (98% purity), and CuO ( $\geq 99\%$  purity). The oxides were pre-annealed for 4 h at 600 °C to remove adsorbed moisture and CO<sub>2</sub>, then taken in stoichiometric amounts and dissolved in nitric acid ( $\geq 65\%$  purity). The salt Ni(CH<sub>3</sub>COO)<sub>2</sub>·4H<sub>2</sub>O was dissolved in distilled water. The resulting solutions were then combined, and glycerol (99.6% purity) was subsequently added to the mixture to serve the dual functions of a chelating agent and an organic fuel. The required amount of glycerol was determined from the redox reaction equation, wherein the nitrate ion serves as the oxidizing agent.

The resulting precursor was heated on a hot plate until the water had evaporated completely, thereby initiating the combustion process. The resulting powder was then subjected to annealing at 900 °C for 12 h to remove any residual organic matter. The synthesis of the materials was conducted in two stages, at 1000 °C for 12 h and at 1100 °C for 12 h, with intermediate grinding occurring between the stages. Details of the synthesis procedure are given in [57].

The phase purity of the Pr<sub>1.6</sub>Ca<sub>0.4</sub>Ni<sub>1-y</sub>Cu<sub>y</sub>O<sub>4+δ</sub> ( $y = 0.0$ – $0.4$ ) materials was determined after the final step by powder X-ray diffraction (XRD) analysis using a Shimadzu XRD-7000 diffractometer (Japan) with a graphite monochromator with Cu K $\alpha$ 1 radiation at room temperature in air. The

XRD patterns were obtained over the angle range of  $10 < 2\theta < 90$  with a step size of  $0.02^\circ$  and an exposure time of 5 s at each point.

Given that the combustion products were typically highly agglomerated, the obtained powders were thoroughly dispersed in an agate mortar with the addition of ethanol to achieve a specific surface area ( $S_{BET}$ ) of no less than  $1 \text{ m}^2 \text{ g}^{-1}$ . The Brunauer-Emmett-Teller (BET) method was employed to determine  $S_{BET}$  values, utilizing a SORBI N.4.1 analyzer (Meta, Russia).

The temperature behavior of the oxygen overstoichiometry,  $\delta$ , in the  $\text{Pr}_{1.6}\text{Ca}_{0.4}\text{Ni}_{1-y}\text{Cu}_y\text{O}_{4+\delta}$  ( $y = 0.0-0.4$ ) materials and the absolute oxygen content were determined via thermogravimetric analysis (TGA) by heating the samples in air and in a  $\text{H}_2+\text{Ar}$  gas mixture (volume ratio of 1:1), respectively. The weight loss measurements were conducted using an STA 449 F3 Jupiter thermal analyzer (Netzsch, Germany). Prior to measurements, the oxygen content in the powder samples was equilibrated in dry air at  $1100^\circ\text{C}$  for 1 h inside the device with slow heating and cooling. The samples were then heated in air to  $1000^\circ\text{C}$  at a rate of  $2^\circ\text{C}/\text{min}$  to measure the weight loss, from which the temperature dependence of the change in  $\delta$  was subsequently determined. The powders were cooled and then heated to  $1000^\circ\text{C}$  in a  $\text{H}_2+\text{Ar}$  gas mixture (volume ratio of 1:1) until complete reduction. On the basis of the results of both experiments, the  $\delta$  values at room temperature and  $700^\circ\text{C}$  were determined. The experimental procedure was established based on the data obtained for the Cu-doped PNO (Supplementary data, Figure S1).

The oxygen mobility of the samples was investigated via the temperature-programmed isotope exchange of oxygen (TPIE) with  $\text{C}^{18}\text{O}_2$  in a flow reactor. The samples sintered at  $1100^\circ\text{C}$  (Table 1, 50 mg weight) were pelletized under a pressure of 400 MPa, then ground and sieved in order to obtain 0.25–0.5 mm fraction. The true density of the samples was measured via hydrostatic weighting. The bulk density, which is the geometric density of the fraction, was calculated by dividing the mass of the fraction by the volume which it occupied.

The samples were loaded into a quartz tubular reactor (inner diameter of 3 mm). The samples were pretreated in a flow of  $\text{He} + 1\% \text{ O}_2$  (flow rate of 25 ml/min) at  $700^\circ\text{C}$  for 0.5 h and then cooled. The TPIE experiments were performed in  $\text{He} + 1\% \text{ C}^{18}\text{O}_2 + 1\% \text{ Ar}$  (flow rate of 25 ml/min)

while heating from  $50^\circ\text{C}$  to  $800^\circ\text{C}$  with a ramp rate of  $5^\circ\text{C}/\text{min}$ . The gas phase composition at the reactor outlet was analyzed by a QMS 200 (Stanford Research Systems, USA) mass spectrometer. The  $^{18}\text{O}$  atomic fraction ( $\alpha$ ) and  $\text{C}^{16}\text{O}^{18}\text{O}$  molecular fraction ( $f_{16-18}$ ) in gas phase dependences were used for calculations of isotope exchange kinetic parameters via mathematical modeling.

## 3. Results and Discussion

### 3.1. Structure

The analysis of the X-ray diffraction data of the as-synthesized  $\text{Pr}_{1.6}\text{Ca}_{0.4}\text{Ni}_{1-y}\text{Cu}_y\text{O}_{4+\delta}$  powder samples reveals the formation of homogeneous complex oxide phases across the entire range of dopant concentrations from  $y = 0.0-0.4$  (PCNO, PCNCO01–PCNCO04). The XRD patterns are presented in Figure 1. All of the obtained materials possess an orthorhombic structure with the  $Bmab$  space group. The refinement of the unit cell parameters was carried out using the Rietveld full-profile analysis method using the FullProf Suite software (presented in Table 2). The theoretical density of the powders,  $\rho_{\text{XRD}}$ , was calculated as follows (Equation 1) [60]:

$$\rho_{\text{XRD}} = \frac{MZ}{N_A V} \quad (1)$$

where  $M$  is the molar mass,  $Z$  is the number of formula units in each unit cell (equal to 4 in this case),  $V$  is the unit cell volume, and  $N_A$  is the Avogadro number.

The unit cell parameter  $c$  increases with increasing Cu content in the series, whereas the  $a$  and  $b$  parameters decrease, which can be related to the tendency of Jahn-Teller  $\text{Cu}^{2+}$  ions to form elongated  $\text{CuO}_6$  octahedra [61, 62]. These multidirectional changes result in an increase in the unit cell volume.

**Table 1** Parameters of the samples used for the TPIE  $\text{C}^{18}\text{O}_2$  studies.

Sample	$S_{BET}$ , [ $\text{m}^2/\text{g}$ ]	True density, [ $\text{g}/\text{cm}^3$ ]	Bulk density, [ $\text{g}/\text{cm}^3$ ]
$\text{Pr}_{1.6}\text{Ca}_{0.4}\text{NiO}_{4+\delta}$	1.5	5.76	2.07
$\text{Pr}_{1.6}\text{Ca}_{0.4}\text{Ni}_{0.9}\text{Cu}_{0.1}\text{O}_{4+\delta}$	2.1	5.96	2.31
$\text{Pr}_{1.6}\text{Ca}_{0.4}\text{Ni}_{0.8}\text{Cu}_{0.2}\text{O}_{4+\delta}$	1.3	5.58	1.98
$\text{Pr}_{1.6}\text{Ca}_{0.4}\text{Ni}_{0.7}\text{Cu}_{0.3}\text{O}_{4+\delta}$	1.0	5.62	2.11
$\text{Pr}_{1.6}\text{Ca}_{0.4}\text{Ni}_{0.6}\text{Cu}_{0.4}\text{O}_{4+\delta}$	1.2	5.83	2.09

**Table 2** Goldschmidt tolerance factor ( $t$ ), structure parameters and oxygen content for the PCNCO series.

$y$	0.0	0.1	0.2	0.3	0.4
Sample designation	PCNO	PCNCO01	PCNCO02	PCNCO03	PCNCO04
$t$	0.899	0.886	0.881	0.880	0.877
$a$ , [Å]	5.3537(1)	5.3441(2)	5.3340(3)	5.3270(1)	5.3220(2)
$b$ , [Å]	5.3726(2)	5.3686(3)	5.3626(3)	5.3580(1)	5.3560(2)
$c$ , [Å]	12.3706(3)	12.4166(3)	12.4659(3)	12.5051(4)	12.5521(4)
$V$ , [Å <sup>3</sup> ]	355.82(2)	356.24(1)	356.58(1)	356.98(2)	357.8(2)
$\rho_{\text{XRD}}$ , [g/cm <sup>3</sup> ]	6.803	6.798	6.801	6.802	6.796
$4+\delta$	4.12	4.09	4.02	3.97	4.00

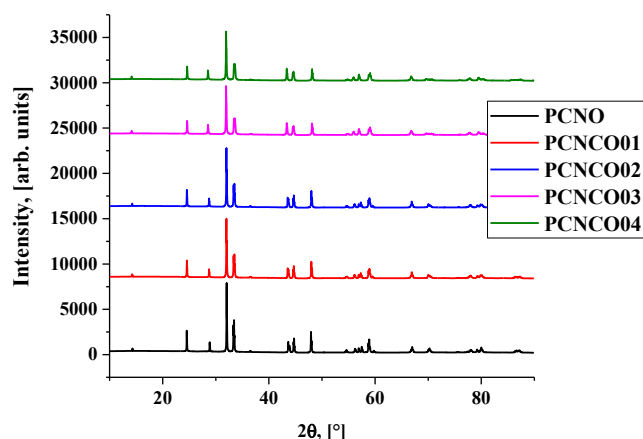


**Figure 1** XRD patterns obtained at room temperature for the as-synthesized PCNCO materials.

In our recent studies, extended data on the structure for  $\text{Pr}_{1.6}\text{Ca}_{0.4}\text{Ni}_{1-y}\text{Cu}_y\text{O}_{4+\delta}$  ( $y = 0.0-0.4$ ) [57],  $\text{Nd}_{1.6}\text{Ca}_{0.4}\text{Ni}_{1-y}\text{Cu}_y\text{O}_{4+\delta}$  ( $y = 0.0-0.4$ ) [47,56] and  $\text{La}_{1.7}\text{Ca}_{0.3}\text{Ni}_{1-y}\text{Cu}_y\text{O}_{4+\delta}$  ( $y = 0.0-0.4$ ) [40] materials, including calculated bond lengths, were presented. Table S1 provides a summary of the structural data for the initial, middle and final compositions of the series of materials ( $y = 0, 0.2$  and  $0.4$  ( $0.3$  in the case of the NCNCO series), PCNO, PCNCO02, PCNCO04, NCNO, NCNCO02, NCNCO03, LCNO, LCNCO02, and LCNCO04, respectively). It can be seen that the tolerance factor,  $t$ , calculated according to Equation S1, decreases slightly with increasing Cu concentration and is in the range of  $0.87 < t < 0.99$ , which is typical of the  $\text{K}_2\text{NiF}_4(T)$ -type structure [63]. A decrease in  $t$  results from the replacement of  $\text{Ni}^{2+}$  by larger cations of  $\text{Cu}^{2+}$  in the series ( $r_{\text{Ni}^{2+_{\text{VI}}}} = 0.69 \text{ \AA}$ ,  $r_{\text{Ni}^{3+_{\text{VI}}(\text{LS})}} = 0.56 \text{ \AA}$ ,  $r_{\text{Ni}^{3+_{\text{VI}}(\text{HS})}} = 0.59 \text{ \AA}$ ,  $r_{\text{Cu}^{2+}} = 0.73 \text{ \AA}$  according to Shannon [64]), which causes an expansion of the  $[\text{Ni}/\text{CuO}_2]^{2-}$  layers, thus destabilizing the structure. Nevertheless, single-phase materials are obtained over the whole concentration range up to  $y = 0.4$  for the Pr/Ca and La/Ca series, confirming the higher solubility of Cu cations and their structures than those of Nd/Ca ( $y = 0.35$ ) [47].

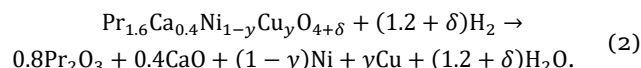
According to the data of the high-temperature XRD study [47,57], the PCNCO and NCNCO materials exhibit an orthorhombic structure at room temperature with the phase transition to a tetragonal structure at temperatures of approximately 180–200 and 300–400 °C, respectively (Table S1).

In Ca-doped layered nickelates, cations occupying the Ln/Ca sites coordinate with four O1 and five O2 ions, whereas in the first coordination sphere of the cations in the Ni sites there are four O1 ions and two O2 ions [65]. Copper cations are able to form elongated  $\text{CuO}_6$  octahedra in place of more regular  $\text{NiO}_6$  octahedra. This can be explained by the preference of  $\text{Cu}^{2+}$  cations for square planar

coordination [66], resulting in an elongated Ni/Cu–O2 bond length and a compressed Ni/Cu–O1 bond length, which is observed in the whole LnCNCO series (Table 2). The replacement of  $\text{Ni}^{2+}$  by  $\text{Cu}^{2+}$  results in an increase in the Ln/Ca–Ln/Ca, Ln/Ca–O1 and Ln/Ca–O2x1 bond lengths, whereas the Ln/Ca–O2x4 bond length decreases. The  $c$  unit cell parameter value, which is the sum of doubled Ln/Ca–O2x1, doubled Ni/Cu–O2, and Ln/Ca–Ln/Ca distances, increases with increasing Cu doping. The Ni/Cu–O1 and Ln/Ca–O2x4 bond lengths, corresponding to the  $a$  and  $b$  parameters, both decrease with increasing doping. Since the Ln/Ca–O2 distance corresponds to the thickness of the  $\text{Ln}(\text{Ca})_2\text{O}_2$  layer, Cu doping may result in faster oxygen migration in the LnCNCO structure.

### 3.2. Oxygen content

The oxygen content in the samples was calculated according to the reaction of the material reduction in a hydrogen-containing atmosphere. For example, for the PCNCO series it can be written as follows (Equation 2):



The  $\delta$  value in the material can be calculated from the change in the mass of the sample in the reducing atmosphere as follows:

$$\delta = \frac{-M_{\text{ox}}}{M_{\text{O}}} + \frac{m_0 M_{\text{red}}}{M_{\text{O}} m_{\text{red}}}, \quad (3)$$

where  $m_0$  and  $m_{\text{red}}$  correspond to the mass of the sample before and after reduction, respectively,  $g$ ;  $M_{\text{ox}}$  is the molar mass of the initial oxide,  $g \text{ mol}^{-1}$ ;  $M_{\text{red}}$  is the total molar mass of the reduction products, considering the coefficients in Equation (2),  $g \text{ mol}^{-1}$ ; and  $M_{\text{O}}$  is the molar mass of the oxygen atom,  $g \text{ mol}^{-1}$ .

At the conventional operation temperature of IT-SOFCs (700 °C), the oxygen content is calculated from the TGA data obtained during heating in air. The resulting dependences for the PCNCO, NCNCO and LCNCO series are presented in Figures 2A, 2B and 2C, respectively.

It is known that the introduction of Ca, which is an acceptor-type dopant for LnNiO, leads to the formation of oxygen vacancies in the perovskite layer. As-formed oxygen vacancies are assumed to be occupied by the nearest interstitial oxygen, as the probability of the coexistence of both in the LnNiO structure is very low [67]. Thus, the overstoichiometric oxygen content in the samples decreases. The total oxygen content values for the LnCNCO samples are listed in Table S1. Despite the lower Ca content for the La-based series (15 mol.% for LCNO and 20 mol. % for PCNO and NCNO), the LCNO sample has the lowest oxygen content, which agrees well with the absolute oxygen content for undoped LnNiO, which was found to be 4.26, 4.24 and



4.16 for NNO, PNO and LNO, respectively [29]. Interestingly, for the PCNO samples with the same dopant level but synthesized via different techniques, the values of oxygen overstoichiometry are remarkably different. For example, for PCNO obtained via nitrate combustion with glycerol, similar to the results of this study, the delta is 0.12, whereas for PCNO obtained via hydroxide coprecipitation it is two times lower [68].

The TGA data presented in Figure 2 clearly demonstrate that the oxygen content in the samples decreases with increasing Cu doping. In the PCNCO series, the samples with  $y \geq 0.2$  become oxygen deficient. The values obtained for Ca/Cu-co-doped PNO are lower than those obtained for Ca [68] and Cu-doped  $\text{Pr}_2\text{NiO}_{4+\delta}$  [50] because both dopants tend to decrease the interstitial oxygen content.

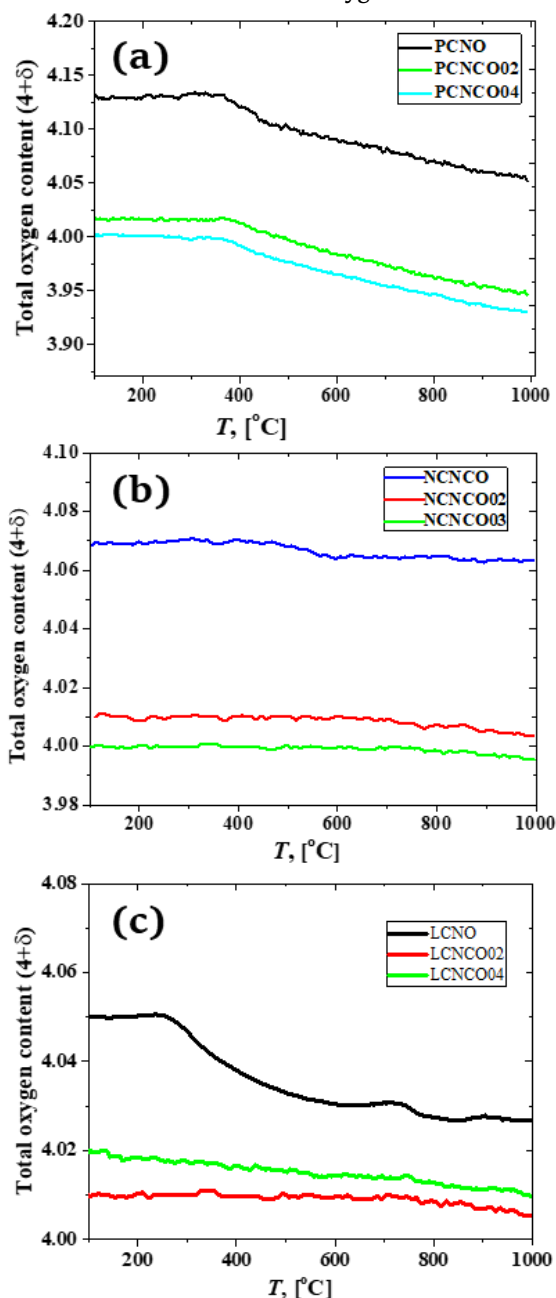


**Figure 2** Total oxygen content in the materials of the PCNCO, NCNCO and LCNCO series, as calculated from the TGA data in air.

In the case of PCNCO, co-doping causes the oxygen content to decrease even faster than that in the NCNCO and LCNCO series, which remain overstoichiometric both at room and at the SOFC operating temperatures. The decrease in the absolute oxygen content can be explained by the fact that copper cations exhibit a lower average oxidation state in isostructural oxide compounds compared to nickel cations, as evident, for example, from the data on the oxygen nonstoichiometry of  $\text{La}_2\text{CuO}_{4+\delta}$  [69] and  $\text{La}_2\text{NiO}_{4+\delta}$  [70] under identical  $p\text{O}_2$ - $T$  conditions, as confirmed by the XPS studies of the PCNCO materials [57].

A further decrease with increasing temperature is related to the release of oxygen from the layered structure of the oxide. In Pr- and Nd-based systems, the release of oxygen results in the orthorhombic-to-tetragonal structure transition. The temperatures of this transition are listed in Table S1.

### 3.3. Conductivity

Conductivity was measured by a four-probe *dc* technique using ceramic samples of a bar shape. The relative densities of the samples, calculated as  $\rho_{\text{exp}}/\rho_{\text{XRD}} \cdot 100\%$ , were in the relatively narrow range of 92–94%, which was achieved by varying the sintering temperature as follows: 1450 °C for Cu-free samples, 1400 °C for  $y = 0.1$ , 1380 °C for  $y = 0.2$ , and 1350 °C for  $y = 0.3$ – $0.4$ . Figure 3 presents a summary of the total conductivity data for LnNiO and LnCNCO collected throughout the studies performed by our group [31, 40, 44, 56, 65, 68].

For convenience, the conductivity values at 700 °C are listed in Table S1.

As shown in Figure 3A, the temperature dependences of the total conductivity show semiconducting behavior at low temperatures, with a maximum at 350–500 °C, followed by a decrease in conductivity. The latter is mostly due to the beginning of active oxygen release from the studied samples, which is accompanied by a decrease in the concentration of electron holes, which are the major charge carriers in the oxides. The temperature of the maximum usually shifts to higher values with increasing doping.

For undoped LnNO, the highest conductivity value is observed for the system with the lowest lanthanide radius. It is known that the transfer of charge carriers in layered nickelates occurs mainly in the equatorial planes of the  $\text{NiO}_6$  octahedra [1]. A decrease in the Ni-O1 bond length with a decrease in the radius of the  $\text{Ln}^{3+}$  ion results in an increase in the intensity of jumps; this is associated with an increase in electrical conductivity and the maximum electrical conductivity attained for the NNO sample.

Depending on the composition of the doped samples, the following dependences are observed: 1) doping with  $\text{Ca}^{2+}$  leads to an increase in electrical conductivity, and 2) co-doping with  $\text{Cu}^{2+}$  results in a decrease in conductivity.

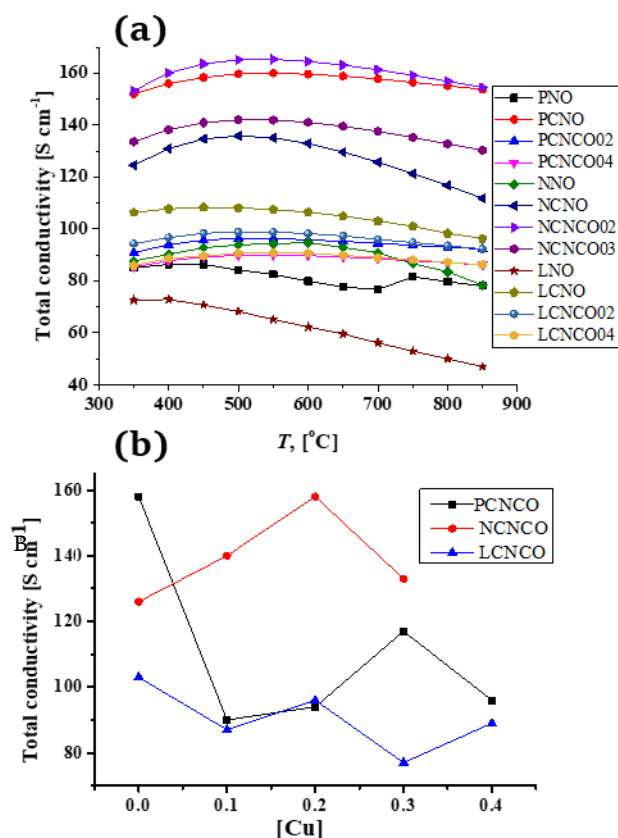


**Figure 3** Total conductivity in air for the LnNO and LnCNCO series (Ln = Pr, Nd, La): temperature dependences (A) and concentration dependences at 700 °C.

The substitution of Ca<sup>2+</sup> for Ln<sup>3+</sup> cations lead to an increase in the concentration of compensating electron holes, which leads to an increase in the conductivity level compared with LnNO due to an increase in the electron component of the total conductivity. Co-doping with Cu results in a decrease in the conductivity of the LaCNCO series (Figure 3B), which correlates well with the literature data [49]. However, for the Nd/Ca and Pr/Ca series (except for PCNO), such a decrease can be observed only for the sample with 40 mol.% copper ( $y = 0.4$ ), which can be explained by several factors: a decrease in the conductivity due to a decrease in the concentration of the electronic charge carriers-electron holes localized on the B-site transition metal cations (i.e., the concentration of Ni<sup>3+</sup>) due to Cu<sup>2+</sup> doping and improved sinterability of the Cu-containing materials. The conduction behavior of Nd- and Pr-based systems may also be affected by the phase transition and the miscibility gap [71, 72].

### 3.4. Oxygen mobility

The TPIE C<sup>18</sup>O<sub>2</sub> curves are given in Figure 4. The isotope exchange process starts at ~250 °C and involves ~90–100% of the total oxygen content of samples, thereby exhibiting favorable oxygen transport characteristics. The  $\alpha(T)$  curves for all the samples possess a few extrema, indicating the presence of multiple oxygen forms with varying isotope substitution rates within the samples.

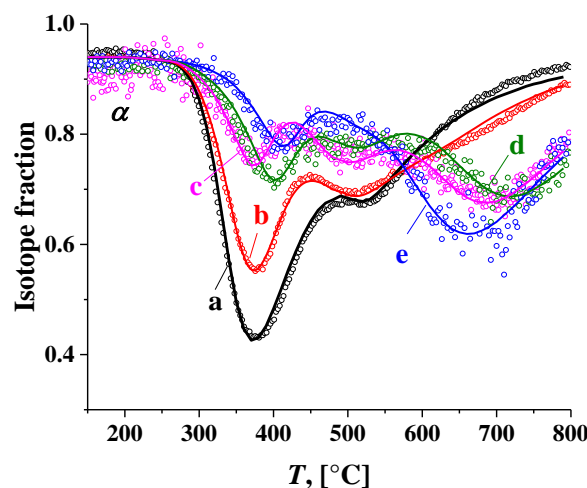


**Figure 4** Temperature-programmed isotope exchange of oxygen with C<sup>18</sup>O<sub>2</sub> in the flow reactor for the Pr<sub>1.6</sub>Cu<sub>0.4</sub>Ni<sub>1-y</sub>Cu<sub>y</sub>O<sub>4+δ</sub> samples,  $y = 0.0$  (a),  $0.1$  (b),  $0.2$  (c),  $0.3$  (d) and  $0.4$  (e). Points – experiment, lines – modeling.

In the case of the Pr<sub>1.6</sub>Ca<sub>0.4</sub>NiO<sub>4+δ</sub> sample, two clearly distinguishable extrema are evident at temperatures of approximately 350 and 540 °C. These extremes correspond to two distinct oxygen forms, which can be designated O<sub>fast</sub> and O<sub>middle</sub>, respectively. For the Pr<sub>1.6</sub>Ca<sub>0.4</sub>Ni<sub>0.9</sub>Cu<sub>0.1</sub>O<sub>4+δ</sub> sample, two extrema are observed at almost the same temperatures. However, the area of the first extremum is found to be lower compared to that of the Pr<sub>1.6</sub>Ca<sub>0.4</sub>NiO<sub>4+δ</sub> sample, indicating that the dynamics of reaching isotope equilibrium are slower. The doping results in a reduction in the amount of fast oxygen, accompanied by the emergence of very slowly substituting forms of oxygen (O<sub>slow</sub>) (at  $y \geq 0.2$ ). As the Cu-content increases, the amount of fast oxygen decreases, leading to a decrease in the overall rate of oxygen substitution.

A mathematical model considering the mechanism of isotope exchange, in which there is a single diffusion channel from the surface into the oxide bulk involving the most mobile oxygen and then subsequent isotope exchange occurs with neighboring, more strongly bound lattice oxygen species, was successfully used for Ca- and Cu-doped lanthanum nickelates [42] and many other complex oxides [12, 13]. However, its application is challenging with respect to the precise representation of the experimental TPIE C<sup>18</sup>O<sub>2</sub> data obtained for the Pr<sub>1.6</sub>Cu<sub>0.4</sub>Ni<sub>1-y</sub>Cu<sub>y</sub>O<sub>4+δ</sub> series. A more accurate description can be achieved via a mathematical model that includes two or three distinct oxygen forms, each characterized by a specific diffusion coefficient value (Figure 5). The estimated fractions of each oxygen form, along with the corresponding diffusion coefficients and activation energy values, are provided in Table 3.

For the Pr<sub>1.6</sub>Ca<sub>0.4</sub>NiO<sub>4+δ</sub> and Pr<sub>1.6</sub>Ca<sub>0.4</sub>Ni<sub>0.9</sub>Cu<sub>0.1</sub>O<sub>4+δ</sub> samples, surface exchange was identified as the limiting stage at temperatures below 300 °C. The surface exchange rate can be described by a mass exchange (or interphase exchange) coefficient  $K$  (Figure 5) since the precise limiting factor is unclear due to the small specific surface area of the samples (Table 1).

**Table 3** Parameters of isotope exchange for  $\text{Pr}_{1.6}\text{Ca}_{0.4}\text{Ni}_{1-y}\text{Cu}_y\text{O}_{4+\delta}$  ( $y = 0.0-0.4$ ) at 423 °C: mass exchange coefficient ( $K$ ), fractions of different oxygen forms ( $\theta$ ), tracer diffusion coefficient ( $D^*$ ), and effective activation energy ( $E_a$ ).

$y$	Surface			Volume							
	$K \cdot 10^4$ , [mol/ (m <sup>2</sup> s)]	$E_a$ , [kJ/ mol]	$\theta$ , [%]	$O_{\text{fast}}$			$O_{\text{middle}}$			$O_{\text{slow}}$	
				$D^* \cdot 10^{11}$ , [cm <sup>2</sup> /s]	$E_a$ , [kJ/ mol]	$\theta$ , [%]	$D^* \cdot 10^{13}$ , [cm <sup>2</sup> /s]	$E_a$ , [kJ/ mol]	$\theta$ , [%]	$D^* \cdot 10^{15}$ , [cm <sup>2</sup> /s]	$E_a$ , [kJ/ mol]
0.0	0.8	160	77	3.6		23	0.6	160	0	-	-
0.1	22	160	40	2.3		30	0.5	160	30 <sup>a</sup>	(0.1÷1)	160
0.2	Not limited		15	4.2	160	25 <sup>a</sup>	(0.2÷2)	160	60	1.0	160
0.3	Not limited		20	1.7		20 <sup>a</sup>	(0.1÷1)	160	60	0.7	160
0.4	Not limited		13	0.7		7 <sup>a</sup>	(0.1÷1)	160	80	1.1	160

<sup>a</sup> These forms of oxygen are actually a set of the oxygen forms close by their mobility. In this case, a range of diffusion coefficient values is estimated.

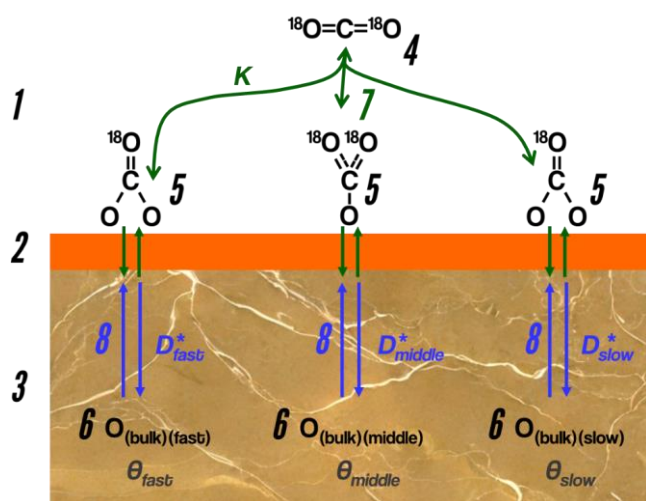


**Figure 5** Schematic illustration of the model of oxygen transport in  $\text{Pr}_{1.6}\text{Ca}_{0.4}\text{Ni}_{1-y}\text{Cu}_y\text{O}_{4+\delta}$ . 1 - gas phase (including pores/voids in the sample), 2 - sample surface, 3 - sample bulk, 4 -  $\text{C}^{18}\text{O}_2$  molecule, 5 - surface carbonate complexes, 6 - bulk oxygen forms with fast, middle and slow transport and fractions of  $\theta_{\text{fast}}$ ,  $\theta_{\text{middle}}$  and  $\theta_{\text{slow}}$ , respectively, 7 - mass exchange between gas and solid phases (including oxygen surface exchange and permeation of the surface layer) characterized by a coefficient  $K$ , 8 - fast, middle and slow diffusion channels characterized by oxygen tracer diffusion coefficients  $D_{\text{fast}}$ ,  $D_{\text{middle}}$  and  $D_{\text{slow}}$ , respectively.

This may be due to the rate of exchange with surface oxygen species, the permeability of the surface layer, or a combination of these factors.

The Arrhenius plots for the oxygen mass exchange ( $K$ ) and tracer diffusion coefficients ( $D^*$ ) are given in Figures 6 and 7, respectively. The higher  $K$  values observed for the  $\text{Pr}_{1.6}\text{Ca}_{0.4}\text{Ni}_{0.9}\text{Cu}_{0.1}\text{O}_{4+\delta}$  sample as compared with those for the  $\text{Pr}_{1.6}\text{Ca}_{0.4}\text{NiO}_{4+\delta}$  one is probably related to variations in the surface heteroexchange rate or permeability of the sample surface layer, which can be caused by the sample surface properties, such as the effective charge of the cations and the contributions of more strongly bound surface oxygen [43], as well as the effects of the sample dispersion and the porous structure [45, 46].

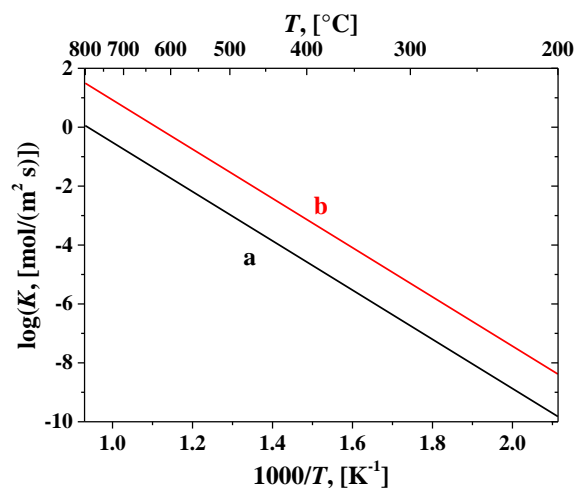


**Figure 6** Arrhenius plots for the mass exchange coefficient acquired for the  $\text{Pr}_{1.6}\text{Ca}_{0.4}\text{Ni}_{1-y}\text{Cu}_y\text{O}_{4+\delta}$  samples from TPIE  $\text{C}^{18}\text{O}_2$  data,  $y = 0.0$  (a) and 0.1 (b).

The oxygen tracer diffusion coefficient values and the contribution of fast oxygen forms tend to decrease with increasing Cu content, which is similar to the trends observed and discussed for Ca- and Cu-doped La [44] and Nd nickelates [47] and can be explained by the variation in highly mobile interstitial oxygen content, since the effective activation energy values remain the same within the calculation error. However, the highest  $D^*$  value for  $O_{\text{fast}}$  is demonstrated for the  $\text{Pr}_{1.6}\text{Ca}_{0.4}\text{Ni}_{0.8}\text{Cu}_{0.2}\text{O}_{4+\delta}$  sample ( $9.4 \cdot 10^{-8}$  cm<sup>2</sup>/s at 700 °C (Figure 7, dependence d), which is slightly higher than that for the Cu-free sample (Figure 7, dependence b).

This maximum  $D^*$  value for  $O_{\text{fast}}$  correlates well with the minimum polarization resistance observed for the  $\text{Pr}_{1.6}\text{Ca}_{0.4}\text{Ni}_{0.8}\text{Cu}_{0.2}\text{O}_{4+\delta}$  electrode with a collector ( $0.27 \Omega \text{ cm}^2$  at 700 °C) in our recent study, which is lower than the values obtained for PCNO ( $0.64 \Omega \text{ cm}^2$  [57],  $0.92 \Omega \text{ cm}^2$  [68]) and PNO ( $0.72 \Omega \text{ cm}^2$  [68]). On the other hand, the contribution of  $O_{\text{fast}}$  is lower than that of the  $\text{Pr}_{1.6}\text{Ca}_{0.4}\text{Ni}_{0.7}\text{Cu}_{0.3}\text{O}_{4+\delta}$  sample (Table 2).

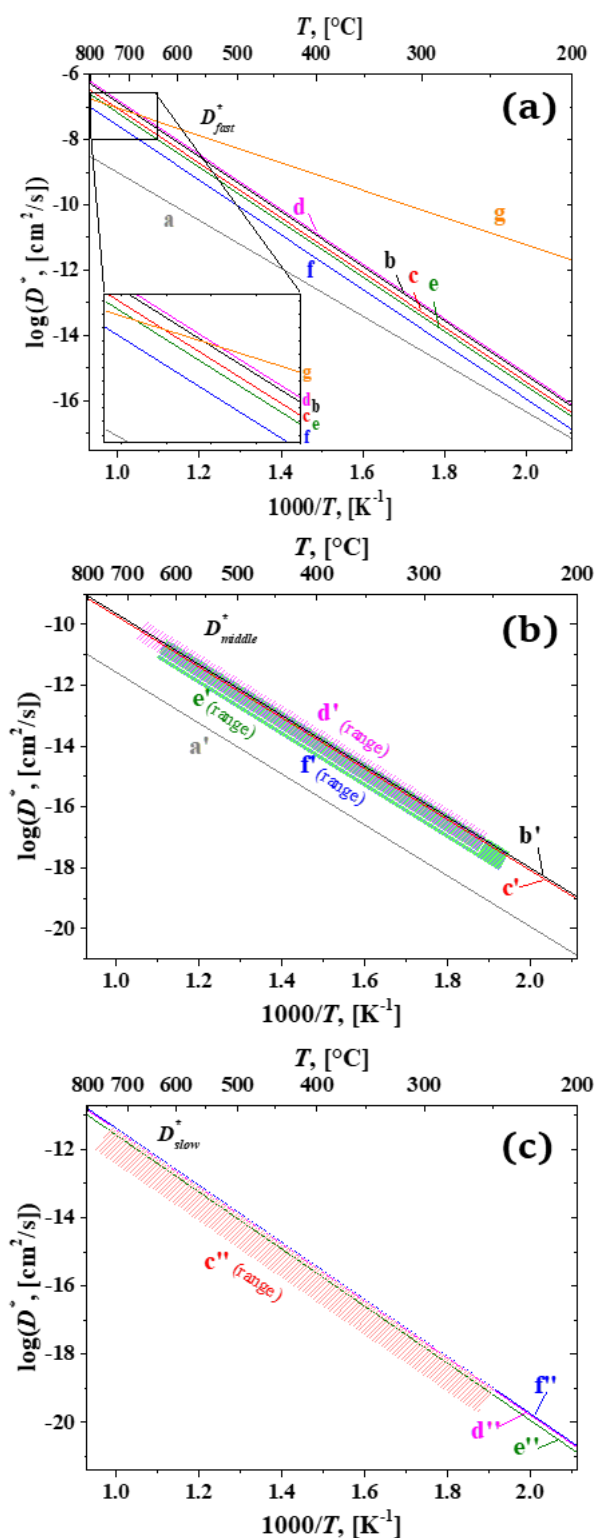


**Figure 7** Arrhenius plots for the oxygen tracer diffusion coefficient (Fast (A), Middle (B) and Low (C)) acquired for the  $\text{Pr}_{1.6}\text{Ca}_{0.4}\text{Ni}_{1-y}\text{Cu}_{0.4}\text{O}_{4+\delta}$  samples from the TPIE  $\text{C}^{18}\text{O}_2$  data,  $y = 0.0$  (a, a') [68], 0.0 (b, b'), 0.1 (c, c'), 0.2 (d, d'), 0.3 (e, e') and 0.4 (f, f'), compared with the undoped  $\text{Pr}_2\text{NiO}_{4+\delta}$  (g) [68].

Nevertheless, the related electrode demonstrates worse electrochemical properties in the series of Cu-doped PCNO [57], which may be related to the nonoptimized electrode microstructure. From our point of view, the potential of this material should be further explored, as it was performed for  $\text{Pr}_{1.6}\text{Ca}_{0.4}\text{Ni}_{0.6}\text{Cu}_{0.4}\text{O}_{4+\delta}$  [58].

Notably, the diffusion coefficient values for the  $\text{Pr}_{1.6}\text{Ca}_{0.4}\text{NiO}_{4+\delta}$  sample acquired in this work are  $\sim 2$  orders of magnitude greater than those of the sample with the same composition studied earlier [68], which can be associated with differences in synthesis technique and sintering temperature. These preparation parameters affect not only the dispersity of the powders but also the interstitial oxygen content, which is a crucial factor influencing the oxygen kinetic features. The  $\delta$  values obtained for the  $\text{Pr}_{1.6}\text{Ca}_{0.4}\text{NiO}_{4+\delta}$  sample synthesized via coprecipitation of hydroxides [68] and nitrate combustion in this study are 0.06 and 0.12, respectively. As expected, the higher interstitial oxygen content results in superior diffusion properties (Table 4).

The oxygen tracer diffusion coefficient values corresponding to  $O_{\text{fast}}$  are lower than those of undoped  $\text{Pr}_2\text{NiO}_{4+\delta}$  (Figure 7, dependence g) at low and intermediate temperatures; however, they are comparable or even greater at high temperatures. Nevertheless, the oxygen mobility remains high for all samples in the PCNCO series ( $D_{\text{fast}} \sim 10^{-8} \text{ cm}^2/\text{s}$  at 700  $^\circ\text{C}$ ), which makes them promising materials for practical application. For comparison, the data for Cu-doped LnCNO are summarized in Table 4 and compared with the data obtained for undoped oxides. It is seen that in the NCNCO series, a weak dependence of the diffusion properties on the Cu content was observed; all the samples demonstrate  $D_{\text{fast}}$  values of  $\sim 10^{-9} \text{ cm}^2/\text{s}$  at 700  $^\circ\text{C}$ , whereas for the LCNCO series, the  $D_{\text{fast}}$  is one order of magnitude lower.

It is well known that the oxygen transport in Ruddlesden-Popper phases proceeds via a cooperative mechanism involving both regular and highly mobile interstitial oxygen through interstitialcy movement [26, 30, 75, 76]. Doping A-site with larger cations such as Ca leads to the hampering of the cooperative mechanism of oxygen migration due to the effect of steric hindrances for an oxygen jump and a decrease in the interstitial oxygen content, leading to decreasing  $D^*$  values and sometimes the emergence of slow diffusion channels, which is discussed in detail in our previous works [14, 29, 35, 68, 77]. Therefore, the PCNO samples, both of which were studied earlier [28] (Figure 7, dependence a) and in this work (Figure 7, dependence b), have two oxygen forms characterized by two different diffusion coefficients.  $O_{\text{fast}}$  characterized by  $D_{\text{fast}}$  apparently corresponds to the motion of oxygen via the cooperative mechanism. Less mobile oxygen form  $O_{\text{middle}}$  probably corresponds to the oxygen moving via the hampered cooperative mechanism [35]. Alternatively,  $O_{\text{slow}}$  can be ascribed to oxygen diffusion via the vacancy mechanism in the perovskite layers, which become oxygen deficient at room temperature (with  $\delta$  values equal to -0.03, -0.03 and 0.00 at  $y = 0.2, 0.3$  and 0.4, respectively), and further vacancy formation occurs with increasing temperature. Indeed, in the works [78–81], the formation of oxygen vacancies for first-order RP phases with low, close-to-zero or negative oxygen overstoichiometry  $\delta$  was demonstrated.



**Table 4** Parameters of isotope exchange for  $\text{Ln}_{2-x}\text{Ca}_x\text{Ni}_{1-y}\text{Cu}_y\text{O}_{4+\delta}$  at 700 °C: tracer diffusion coefficient ( $D^*$ ) and effective activation energy ( $E_a$ ) [44, 47, 68, 73, 74].

Sample	Volume						Ref.
	$O_{\text{fast}}$		$O_{\text{middle}}$		$O_{\text{slow}}$		
	$D^*$ , [cm <sup>2</sup> /s]	$E_a$ , [kJ/mol]	$D^*$ , [cm <sup>2</sup> /s]	$E_a$ , [kJ/mol]	$D^*$ , [cm <sup>2</sup> /s]	$E_a$ , [kJ/mol]	
LNO	$2.0 \cdot 10^{-9}$	100	-	-	-	-	[73]
LCNO	$6.5 \cdot 10^{-10}$						
LCNO	$1.4 \cdot 10^{-9}$						
LCNCO01	$1.1 \cdot 10^{-9}$						
LCNCO02	$7.5 \cdot 10^{-10}$	100	-	-	-	-	[44]
LCNCO03	$6.2 \cdot 10^{-10}$						
LCNCO04	$5.0 \cdot 10^{-10}$						
PNO	$6.9 \cdot 10^{-8}$	80	-	-	-	-	[68]
PCNO	$6.1 \cdot 10^{-10}$	140	$1.6 \cdot 10^{-12}$	160	-	-	
PCNO	$8.0 \cdot 10^{-8}$		$1.2 \cdot 10^{-10}$		-	-	
PCNCO01	$5.2 \cdot 10^{-8}$		$1.1 \cdot 10^{-10}$		$\sim 10^{-13}$		
PCNCO02	$9.4 \cdot 10^{-8}$	160	$\sim 10^{-10}$	160	$2.2 \cdot 10^{-12}$	160	This work
PCNCO03	$3.8 \cdot 10^{-8}$		$\sim 10^{-10}$		$1.6 \cdot 10^{-12}$		
PCNCO04	$1.6 \cdot 10^{-8}$		$\sim 10^{-10}$		$2.5 \cdot 10^{-12}$		
NNO	$4.5 \cdot 10^{-8}$	140	-	-	-	-	[74]
NCNO	$9.8 \cdot 10^{-10}$	120					
NCNO							
NCNCO							
NCNCO02	$3.3 \cdot 10^{-9}$	120	-	-	-	-	[47]
NCNCO03							

Additionally, the  $O_{\text{middle}}$  and  $O_{\text{slow}}$  oxygen forms can be associated with the effect of local distortion of the perovskite structure in the vicinity of the Cu cations, which, in turn, can affect the binding energy of oxygen [42]. Notably, despite the higher  $\delta$  value for the first member of the series (PCNO) determined in this study (0.12), the introduction of Cu cations resulted in a more significant decrease in the interstitial oxygen content compared to the NCNCO and LCNCO series of co-doped nickelates, which remain overstoichiometric at room temperature up to  $y = 0.3$  and  $0.4$ , respectively [40, 56]. Nevertheless, the appearance of oxygen vacancies in the perovskite structure of layered oxides can be favorable for electrode performance, as shown in [40].

The oxide ionic conductivity ( $\sigma_i$ ) of the PCNCO series is estimated from  $D^*$  values via the Nernst–Einstein equation (Equation (4)):

$$\sigma_i = \frac{4q_e^2 N_0}{f k_B T} D^*, \quad (4)$$

where  $f$  is the correlation factor (taken to be equal to 1);  $q_e$  is the electronic charge;  $N_0$  is the total concentration of the oxygen ions in the substance; and  $k_B$  is the Boltzmann constant.

The  $\sigma_i$  values tend to decrease with increasing Cu content due to decreasing  $D_{\text{fast}}$  values and  $O_{\text{fast}}$  contributions (Figure 8A). Nevertheless, the values ( $\sim 10^{-3}$ – $10^{-2}$  S/cm at

700 °C) are close to those for other RP phases [74, 82]. It should be also noted that for the PCNCO series the ionic conductivity values are superior to those for NCNCO and LCNCO. For example, for samples with a medium copper content ( $y = 0.2$ ), the ionic conductivity values at 700 °C were evaluated to be  $3.7 \cdot 10^{-3}$ ,  $4.08 \cdot 10^{-4}$  and  $1.05 \cdot 10^{-4}$  S/cm for  $\text{Pr}_{1.6}\text{Ca}_{0.4}\text{Ni}_{0.8}\text{Cu}_{0.2}\text{O}_{4+\delta}$ ,  $\text{Nd}_{1.6}\text{Ca}_{0.4}\text{Ni}_{0.8}\text{Cu}_{0.2}\text{O}_{4+\delta}$  and  $\text{La}_{1.7}\text{Ca}_{0.3}\text{Ni}_{0.8}\text{Cu}_{0.2}\text{O}_{4+\delta}$ , respectively.

When the oxide ionic conductivity is compared with the total conductivity [57], one can conclude that electronic transport predominates ( $O^{2-}$  transfer number  $\sim 10^{-3}$  at 700 °C); hence, the ambipolar conductivity,  $\sigma_{\text{amb}} = \frac{\sigma_e \sigma_i}{(\sigma_e + \sigma_i)}$ , can be estimated to be almost equal to the oxide ionic conductivity. Hence, the ambipolar conductivity value series can be considered to be high enough for practical application.

### 3.5. Electrochemical properties

Table 5 summarizes the electrochemical properties of LnCNCO-based electrodes in contact with  $\text{Ce}_{0.2}\text{Sm}_{0.2}\text{O}_{1.9}$  electrolyte, which were recently studied elsewhere [40, 47, 57]. It can be seen, that the electrodes with PCNCO functional layers demonstrate the most promising characteristics, which was supported by the enhanced oxygen kinetic properties obtained in this study. On the contrary, a correlation with the electrical properties of the materials is not apparent. This is a distinctive feature of the MIEC materials [59].

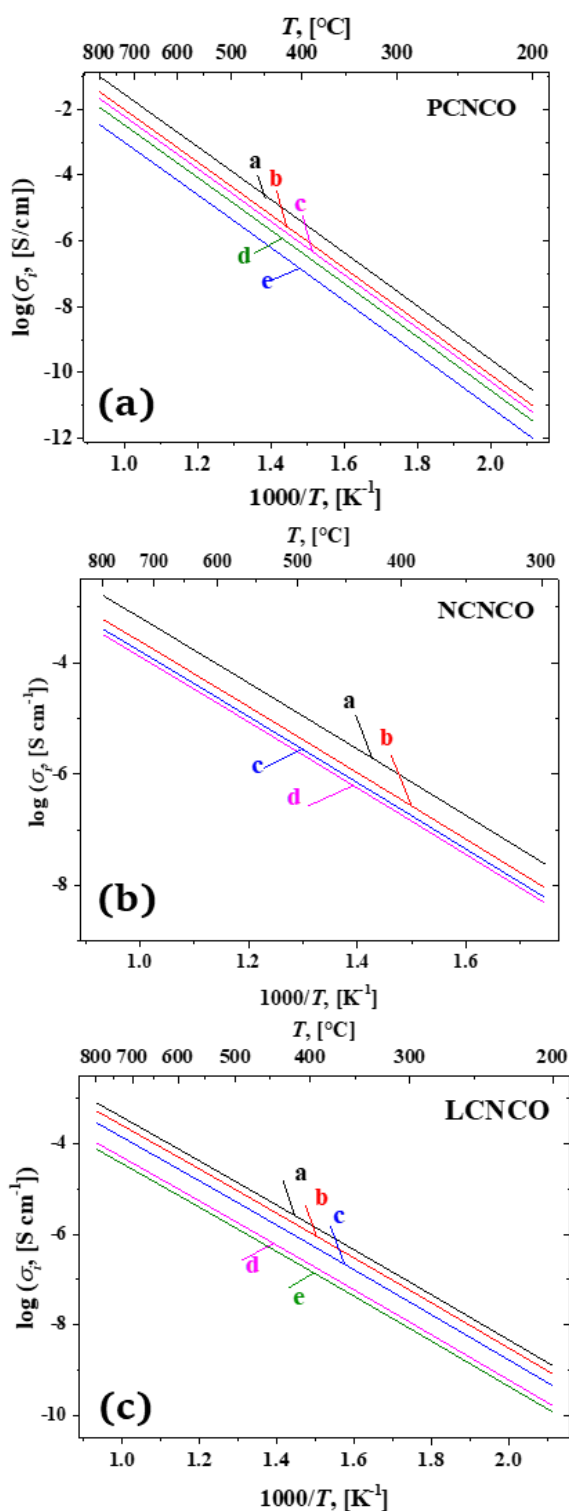


**Figure 8** Oxide ionic conductivity estimated from the isotope exchange data: A) PCNCO,  $y = 0.0$  (a),  $0.1$  (b),  $0.2$  (c),  $0.3$  (d) and  $0.4$  (e); B) NCNCO,  $y = 0.0$  (a),  $0.1$  (b),  $0.2$  (c),  $0.3$  (d) and C) LCNCO,  $y = 0.0$  (a),  $0.1$  (b),  $0.2$  (c),  $0.3$  (d) and  $0.4$  (e).

The analysis of the data presented in Table 5 shows that the electrodes with the PCNCO functional layers exhibited the lowest polarization resistance at  $y = 0.1$  and  $0.2$  ( $1.31$  and  $1.36 \Omega \text{ cm}^2$  at  $700 \text{ }^\circ\text{C}$ , respectively [57]). In contrast, the polarization resistance of the LCNCO electrodes demonstrated an increase at low Cu content ( $y \leq 0.2$ ), followed by a subsequent decrease. Therefore, the LCNCO4 electrode

exhibited the optimal performance in the LCNCO series ( $2.01 \Omega \text{ cm}^2$  at  $700 \text{ }^\circ\text{C}$ , [40]). The lowest value in the NCNCO series was observed at  $y = 0.2$  ( $5.70 \Omega \text{ cm}^2$  at  $700 \text{ }^\circ\text{C}$ , [47]). The application of a highly conductive oxide collector based on  $\text{LaNi}_{0.6}\text{Fe}_{0.4}\text{O}_{3-\delta}$  was found to increase the electrode performance due to better current distribution across the electrode volume. As, for example, for the PCNCO2 electrode, the application of the collector allowed decreasing  $R_p$  by approximately four times, down to  $0.27 \Omega \text{ cm}^2$  at  $700 \text{ }^\circ\text{C}$ .

Moreover, as we have demonstrated recently [57], the PCNCO electrodes with LNF collector may be successfully used in contact with proton-conducting electrolytes, exhibiting the  $R_p$  values in the range of  $0.19$ – $0.21 \Omega \text{ cm}^2$  at  $700 \text{ }^\circ\text{C}$  [57].

#### 4. Limitations

The assumptions on the oxygen transport mechanisms for each oxygen form for the studied materials are based on the experimental data as well as the data presented in the literature, including the authors' previous works. However, elucidating the nature of these oxygen forms and details of their migration pathways requires further studies, which can be carried out in the future.

#### 5. Conclusions

This work continues a series of investigations concerning the physicochemical properties, oxygen diffusion and electrochemical performance of  $\text{Ln}_{2-x}\text{Ca}_x\text{Ni}_{1-y}\text{Cu}_y\text{O}_{4+\delta}$  ( $\text{Ln} = \text{Pr}, \text{Nd}, \text{La}$ ) materials. In particular, this study aimed to investigate the oxygen content and diffusion in  $\text{Pr}_{1.6}\text{Ca}_{0.4}\text{Ni}_{1-y}\text{Cu}_y\text{O}_{4+\delta}$  ( $y = 0.0$ – $0.4$ ) oxides obtained via nitrate combustion with glycerol as a fuel. The materials were found to exhibit an orthorhombic structure, related to the absolute oxygen content in the range of  $4.15$ – $3.97$ . The oxygen mobility in the samples was investigated via temperature-programmed isotope exchange of oxygen (TPIE) with  $\text{C}^{18}\text{O}_2$  in a flow reactor. The obtained curves, comprising few extrema, were fitted via a mathematical model that included two or three distinct oxygen forms, each characterized by a specific diffusion coefficient value: (1)  $\text{O}_{\text{fast}}$ , characterized by  $D_{\text{fast}}$  corresponding to the oxygen moving via the cooperative mechanism, (2)  $\text{O}_{\text{middle}}$ , corresponding to the oxygen moving via a hampered cooperative mechanism, and (3)  $\text{O}_{\text{slow}}$ , ascribed to the oxygen diffusion via a vacancy mechanism in the perovskite layers, which became oxygen deficient at IT-SOFC operating temperatures. The oxygen tracer diffusion coefficient values and the contribution of fast oxygen forms tend to decrease with increasing Cu content, which is similar to the trends observed and discussed for Ca- and Cu-co-doped La and Nd nickelates in our recent studies. These features can be explained by the variation in the highly mobile interstitial oxygen content, since the effective activation energy values remained approximately the same within the calculation error.

**Table 5** Polarization resistance of the electrodes with  $\text{Ln}_{2-x}\text{Ca}_x\text{Ni}_{1-y}\text{Cu}_y\text{O}_{4+\delta}$  functional layers measured in symmetrical cells with the  $\text{Ce}_{0.8}\text{Sm}_{0.2}\text{O}_{1.9}$  electrolyte (at 700 °C in air). Electrodes without and with a collector layer based on  $\text{LaNi}_{0.4}\text{Fe}_{0.6}\text{O}_{3-\delta}$  (LNF) are presented [40, 47, 57, 58, 73, 74, 77, 83].

Electrode FL	without collector		with LNF collector		Ref.
	$R_p$ , [ $\Omega \text{ cm}^2$ ]	$E_a$ , [kJ/mol]	$R_p$ , [ $\Omega \text{ cm}^2$ ]	$E_a$ , [kJ/mol]	
$\text{La}_2\text{NiO}_{4+\delta}$			0.57	105	
$\text{La}_{1.7}\text{Ca}_{0.3}\text{NiO}_{4+\delta}$			4.01	102	[73]
$\text{La}_{1.7}\text{Ca}_{0.3}\text{NiO}_{4+\delta}$	10.52	162			
$\text{La}_{1.7}\text{Ca}_{0.3}\text{Ni}_{0.9}\text{Cu}_{0.1}\text{O}_{4+\delta}$	14.36	139			
$\text{La}_{1.7}\text{Ca}_{0.3}\text{Ni}_{0.8}\text{Cu}_{0.2}\text{O}_{4+\delta}$	12.76	150			[40]
$\text{La}_{1.7}\text{Ca}_{0.3}\text{Ni}_{0.7}\text{Cu}_{0.3}\text{O}_{4+\delta}$	6.87	138			
$\text{La}_{1.7}\text{Ca}_{0.3}\text{Ni}_{0.6}\text{Cu}_{0.4}\text{O}_{4+\delta}$	2.01	133	2.65	140	
$\text{Pr}_2\text{NiO}_{4+\delta}$			0.72		
$\text{Pr}_{1.6}\text{Ca}_{0.4}\text{NiO}_{4+\delta}$			0.93		[77]
$\text{Pr}_2\text{NiO}_{4+\delta}$			0.42	112	
$\text{Pr}_{1.6}\text{Ca}_{0.4}\text{NiO}_{4+\delta}$			0.74	141	[83]
$\text{Pr}_{1.6}\text{Ca}_{0.4}\text{NiO}_{4+\delta}$	1.48	129	0.64	118	
$\text{Pr}_{1.6}\text{Ca}_{0.4}\text{Ni}_{0.9}\text{Cu}_{0.1}\text{O}_{4+\delta}$	1.31	131			
$\text{Pr}_{1.6}\text{Ca}_{0.4}\text{Ni}_{0.8}\text{Cu}_{0.2}\text{O}_{4+\delta}$	1.36	121	0.27	117	[57]
$\text{Pr}_{1.6}\text{Ca}_{0.4}\text{Ni}_{0.7}\text{Cu}_{0.3}\text{O}_{4+\delta}$	1.65	116			
$\text{Pr}_{1.6}\text{Ca}_{0.4}\text{Ni}_{0.6}\text{Cu}_{0.4}\text{O}_{4+\delta}$	1.48	92	0.37	77	
$\text{Pr}_{1.6}\text{Ca}_{0.4}\text{Ni}_{0.6}\text{Cu}_{0.4}\text{O}_{4+\delta}$	0.60	86	0.38	99	[58]
$\text{Nd}_2\text{NiO}_{4+\delta}$			0.71	116	
$\text{Nd}_{1.6}\text{Ca}_{0.4}\text{NiO}_{4+\delta}$			0.38	111	[74]
$\text{Nd}_{1.6}\text{Ca}_{0.4}\text{NiO}_{4+\delta}$	12.28	98	4.21		
$\text{Nd}_{1.6}\text{Ca}_{0.4}\text{Ni}_{0.9}\text{Cu}_{0.1}\text{O}_{4+\delta}$	10.55	117	3.81		
$\text{Nd}_{1.6}\text{Ca}_{0.4}\text{Ni}_{0.8}\text{Cu}_{0.2}\text{O}_{4+\delta}$	5.70	102	3.32		[47]
$\text{Nd}_{1.6}\text{Ca}_{0.4}\text{Ni}_{0.7}\text{Cu}_{0.3}\text{O}_{4+\delta}$	15.69	151	6.91		

The highest  $D^*$  value for  $O_{\text{fast}}$  was demonstrated for the  $\text{Pr}_{1.6}\text{Ca}_{0.4}\text{Ni}_{0.8}\text{Cu}_{0.2}\text{O}_{4+\delta}$  sample, which was  $9.4 \cdot 10^{-8} \text{ cm}^2/\text{s}$  at 700 °C. Co-doping with Cu results in a decrease in the conductivity of the LaCNCO series; however, for the Pr/Ca and Nd/Ca series, such a decrease was observed only for the samples with 40 mol.% copper ( $y=0.4$ ), which can be explained by several factors, such as a decrease in the conductivity due to the reduction in the concentration of the electronic charge carriers and electron holes localized on the B-site transition metal cations (i.e., the concentration of  $\text{Ni}^{3+}$ ) due to  $\text{Cu}^{2+}$  doping and improved sinterability of the samples from the Cu-containing materials. Despite the decrease in conductivity, an increase in the electrochemical performance was demonstrated for the Pr-based electrodes with moderate calcium and copper contents ( $x=0.4$ ,  $y=0.2$ ). This enhancement was observed for the La-based series only at  $y=0.4$ , whereas the performance of the Nd-based electrodes co-doped with Ca and Cu was inferior to that of the undoped material, which can be explained by the non-optimized electrode microstructure.

## • Supplementary materials

This manuscript contains supplementary materials, which are available on the corresponding online page.

## • Funding

Oxygen isotope exchange studies and mathematical modeling of the results were performed in the framework of the budget projects of the Boreskov Institute of Catalysis, Siberian Branch, Russian Academy of Sciences (projects FWUR-2024-0033 and FWUR-2024-0038, respectively). Synthesis of the materials and their characterization was done using the equipment of the Shared Access Center “Composition of compounds” and the Collaborative Usage Center “Ural-M” in the framework of the State Assignment for the Institute of High Temperature Electrochemistry (project 122020100324-3) and Institute of Metallurgy, Ural Branch, Russian Academy of Sciences.

## ● Acknowledgments

The authors are grateful personally to Artem Tarutin (IHTE UB RAS) and Elena Filonova (UrFU) for the treatment and fruitful discussion of the experimental TGA and XRD data.

## ● Author contributions

Conceptualization: V.S., E.P.

Data curation: E.S., S.P.

Formal Analysis: E.S., T.Z., E.P.

Investigation: N.E., T.Z., S.P., Y.F.

Methodology: E.S.,

Resources: T.Z.

Supervision: V.S.

Visualization: N.E., E.S., E.P.

Writing – original draft: N.E., E.S., E.P.

Writing – review & editing: V.S., E.P.

## ● Conflict of interest

The authors declare that they have no conflicts of interest.

## ● Additional information

Scopus author IDs:

Vladislav Sadykov, Scopus ID [7006677003](https://orcid.org/0000-0002-7006-6700),  
[57200684813](https://orcid.org/0000-0002-5720-0684);

Nikita Ereemeev, Scopus ID [55645818400](https://orcid.org/0000-0002-5564-5818);

Ekaterina Sadovskaya, Scopus ID [57202034821](https://orcid.org/0000-0002-5720-2034),  
[57204295192](https://orcid.org/0000-0002-5720-4295);

Tatiana Zhulanova, Scopus ID [57220164187](https://orcid.org/0000-0002-5722-0164);

Sergey Pikalov, Scopus ID [6603186623](https://orcid.org/0000-0002-6603-1866);

Yulia Fedorova, Scopus ID [41461339800](https://orcid.org/0000-0002-4146-1339);

Elena Pikalova, Scopus ID [16242376500](https://orcid.org/0000-0002-1624-2376).

Websites:

Federal Research Center Boreskov Institute of Catalysis  
SB RAS <https://en.catalysis.ru/>;

Institute of High-Temperature Electrochemistry UB  
RAS, <https://ihte.ru/>;

Ural Federal University, <https://urfu.ru/en/>;

Institute of Metallurgy UB RAS, <http://www.imet-uran.ru/>.

## References

- Tarutin AP, Lyagaeva JG, Medvedev DA, Bi L, Yaremchenko AA. Recent advances in layered  $\text{Ln}_2\text{NiO}_{4+\delta}$  nickelates: Fundamentals and prospects of their applications in protonic ceramic fuel and electrolysis cells. *J Mater Chem A*. 2021;9(1):154–95. doi:[10.1039/D0TA08132A](https://doi.org/10.1039/D0TA08132A)
- Chun O, Jamshaid F, Khan MZ, Gohar O, Hussain I, Zhang Y, Zheng K, Saleem M, Motola M, Hanif MB. Advances in low-temperature solid oxide fuel cells: An explanatory review. *J Power Sources*. 2024;610:234719. doi:[10.1016/j.jpowsour.2024.234719](https://doi.org/10.1016/j.jpowsour.2024.234719)
- Baratov S, Filonova E, Ivanova A, Hanif MB, Irshad M, Khan MZ, Motola M, Rauf S, Medvedev D. Current and further trajectories in designing functional materials for solid oxide electrochemical cells: A review of other reviews. *J Energy Chem* 2024;94:302–31. doi:[10.1016/j.jechem.2024.02.047](https://doi.org/10.1016/j.jechem.2024.02.047)
- Yatoo MA, Skinner SJ. Ruddlesden-Popper phase materials for solid oxide fuel cell cathodes: A short review. *Mater Today Proc*. 2022;56(6):3747–54. doi:[10.1016/j.matpr.2021.12.537](https://doi.org/10.1016/j.matpr.2021.12.537)
- Tarutin AP, Filonova EA, Ricote S, Medvedev DA, Shao Z. Chemical design of oxygen electrodes for solid oxide electrochemical cells: A guide. *Sustain Energy Technol Assessments*. 2023;57:103185. doi:[10.1016/j.seta.2023.103185](https://doi.org/10.1016/j.seta.2023.103185)
- Chronos A, Goulatis IL, Solovjov A, Vovk RV. The evolution of solid oxide fuel cell materials. *Appl Sci*. 2023;14(1):69. doi:[10.3390/app14010069](https://doi.org/10.3390/app14010069)
- Morales-Zapata MA, Larrea A, Laguna-Bercero MA. Lanthanide nickelates for their application on solid oxide cells. *Electrochim Acta*. 2023;444:141970. doi:[10.1016/j.electacta.2023.141970](https://doi.org/10.1016/j.electacta.2023.141970)
- Pikalova EYu, Guseva EM, Filonova EA. Short review on recent studies and prospects of application of rare-earth-doped  $\text{La}_2\text{NiO}_{4+\delta}$  as air electrodes for solid-oxide electrochemical cells. *EM&T*. 2023;2(4):20232025. doi:[10.15826/elmattech.2023.2.025](https://doi.org/10.15826/elmattech.2023.2.025)
- Nechache A, Hody S. Alternative and innovative solid oxide electrolysis cell materials: A short review. *Renew Sustain Energy Rev*. 2021;149:111322. doi:[10.1016/j.rser.2021.111322](https://doi.org/10.1016/j.rser.2021.111322)
- Danilov N, Lyagaeva J, Vdovin G, Pikalova E, Medvedev D. Electricity/hydrogen conversion by the means of a protonic ceramic electrolysis cell with  $\text{Nd}_2\text{NiO}_{4+\delta}$ -based oxygen electrode. *Energy Convers Manage*. 2018;172:129–37. doi:[10.1016/j.enconman.2018.07.014](https://doi.org/10.1016/j.enconman.2018.07.014)
- Li W, Guan B, Ma L, Hu S, Zhang N, Liu X. High performing triple-conductive  $\text{Pr}_2\text{NiO}_{4+\delta}$  anode for proton-conducting steam solid oxide electrolysis cell. *J Mater Chem A*. 2018;6(37):18057–66. doi:[10.1039/C8TA04018D](https://doi.org/10.1039/C8TA04018D)
- Tarutin AP, Gilev AR, Baratov SA, Vdovin GK, Medvedev DA. Ba-doped  $\text{Pr}_2\text{NiO}_{4+\delta}$  electrodes for proton-conducting electrochemical cells. Part 3: Electrochemical applications. *Int J Hydrog Energy*. 2024;60:261–71. doi:[10.1016/j.ijhydene.2024.02.173](https://doi.org/10.1016/j.ijhydene.2024.02.173)
- Wolf SE, Winterhalder FE, Vibhu V, (Bert) de Haart LGJ, Guillon O, Eichel R-A, Menzler NH. Solid oxide electrolysis cells – current material development and industrial application. *J Mater Chem A*. 2023;11(34):17977–8028. doi:[10.1039/D3TA02161K](https://doi.org/10.1039/D3TA02161K)
- Sadykov V, Pikalova E, Sadovskaya E, Shlyakhtina A, Filonova E, Ereemeev N. Design of mixed ionic-electronic materials for permselective membranes and solid oxide fuel cells based on their oxygen and hydrogen mobility. *Membranes*. 2023;13(8):698. doi:[10.3390/membranes13080698](https://doi.org/10.3390/membranes13080698)
- Sadykov V, Ereemeev N, Sadovskaya E, Bepalko Yu, Simonov M, Arapova M, Smal E. Nanomaterials with oxygen mobility for catalysis of biofuels transformation into syngas, SOFC and oxygen/hydrogen separation membranes: Design and performance. *Catal Today*. 2023;423:113936. doi:[10.1016/j.cattod.2022.10.018](https://doi.org/10.1016/j.cattod.2022.10.018)
- Qu L, Papaioannou EI. Development of mixed ionic and electronic conducting materials for gas separation membranes: A critical overview. *Chem Eng J*. 2024;496:153791. doi:[10.1016/j.cej.2024.153791](https://doi.org/10.1016/j.cej.2024.153791)
- Zhao Z, Chen G, Escobar Cano G, Kißling PA, Stölting O, Breidenstein B, Polarz S, Bigall NC, Weidenkaff A, Feldhoff A. Multiplying oxygen permeability of a Ruddlesden-Popper oxide by orientation control via magnets. *Angew Chem Int Ed*. 2024;63(8):e202312473. doi:[10.1002/anie.202312473](https://doi.org/10.1002/anie.202312473)
- Escobar Cano G, Zhao Z, Riebesehl F, Stölting O, Breidenstein B, Feldhoff A. Towards the development of textured polycrystalline  $\text{La}_2\text{NiO}_{4+\delta}$  membranes and their oxygen-transporting properties. *J Solid State Electrochem*. 2024. [Cited 2024] doi:[10.1007/s10008-024-05924-4](https://doi.org/10.1007/s10008-024-05924-4)
- Sadykov VA, Sadovskaya EM, Filonova EA, Ereemeev NF, Belyaev VD, Tsvinkinberg TA, Pikalova EYu. Oxide ionic transport features in Gd-doped La nickelates. *Solid State Ionics*. 2020;357:115462. doi:[10.1016/j.ssi.2020.115462](https://doi.org/10.1016/j.ssi.2020.115462)



20. Georgiadis AG, Charisiou ND, Goula MA. A mini-review on lanthanum-nickel-based perovskite-derived catalysts for hydrogen production via the dry reforming of methane (DRM). *Catalysts*. 2023;13(10):1357. doi:[10.3390/catal13101357](https://doi.org/10.3390/catal13101357)
21. Du H, Luo H, Jiang M, Yan X, Jiang F, Chen H. A review of activating lattice oxygen of metal oxides for catalytic reactions: Reaction mechanisms, modulation strategies of activity and their practical applications. *Appl Catal A Gen*. 2023;664:119348. doi:[10.1016/j.apcata.2023.119348](https://doi.org/10.1016/j.apcata.2023.119348)
22. Forslund RP, Alexander CT, Abakumov AM, Johnston KP, Stevenson KJ. Enhanced electrocatalytic activities by substitutional tuning of nickel-based Ruddlesden-Popper catalysts for the oxidation of urea and small alcohols. *ACS Catal*. 2019;9(3):2664–73. doi:[10.1021/acscatal.8b04103](https://doi.org/10.1021/acscatal.8b04103)
23. Park S, Kim Y, Han H, Chung YS, Yoon W, Choi J, Kim WB. In situ exsolved Co nanoparticles on Ruddlesden-Popper material as highly active catalyst for CO<sub>2</sub> electrolysis to CO. *Appl Catal B Environ*. 2019;248:147–56. doi:[10.1016/j.apcatb.2019.02.013](https://doi.org/10.1016/j.apcatb.2019.02.013)
24. Lee D, Lee H. Controlling oxygen mobility in Ruddlesden-Popper oxides. *Materials*. 2017;10(4):368. doi:[10.3390/ma10040368](https://doi.org/10.3390/ma10040368)
25. Xu S, Jacobs R, Morgan D. Factors controlling oxygen interstitial diffusion in the Ruddlesden-Popper oxide La<sub>2-x</sub>Sr<sub>x</sub>NiO<sub>4+δ</sub>. *Chem Mater*. 2018;30(20):7166–77. doi:[10.1021/acs.chemmater.8b03146](https://doi.org/10.1021/acs.chemmater.8b03146)
26. Yang S, Liu G, Lee Y-L, Bassat J-M, Gamon J, Villesuzanne A, Pietras J, Zhou X-D, Zhong Y. A systematic ab initio study of vacancy formation energy, diffusivity, and ionic conductivity of Ln<sub>2</sub>NiO<sub>4+δ</sub> (Ln=La, Nd, Pr). *J Power Sources*. 2023;576:233200. doi:[10.1016/j.jpowsour.2023.233200](https://doi.org/10.1016/j.jpowsour.2023.233200)
27. Chronos A, Yildiz B, Tarancón A, Parfitt D, Kilner JA. Oxygen diffusion in solid oxide fuel cell cathode and electrolyte materials: mechanistic insights from atomistic simulations. *Energy Environ Sci*. 2011;4(8):2774–89. doi:[10.1039/c0ee00717j](https://doi.org/10.1039/c0ee00717j)
28. Boehm E, Bassat J, Dordor P, Mauvy F, Grenier J-C, Stevens Ph. Oxygen diffusion and transport properties in non-stoichiometric Ln<sub>2-x</sub>NiO<sub>4+δ</sub> oxides. *Solid State Ionics*. 2005;176(37–38):2717–25. doi:[10.1016/j.ssi.2005.06.033](https://doi.org/10.1016/j.ssi.2005.06.033)
29. Pikalova EYu, Kolchugin AA, Sadykov VA, Sadovskaya EM, Filonova EA, Ereemeev NF, Bogdanovich NM. Structure, transport properties and electrochemical behavior of the layered lanthanide nickelates doped with calcium. *Int J Hydrog Energy*. 2018;43(36):17373–86. doi:[10.1016/j.ijhydene.2018.07.115](https://doi.org/10.1016/j.ijhydene.2018.07.115)
30. Nirala G, Yadav D, Upadhyay S. Ruddlesden-Popper phase A<sub>2</sub>BO<sub>4</sub> oxides: Recent studies on structure, electrical, dielectric, and optical properties. *J Adv Ceram*. 2020;9(2):129–48. doi:[10.1007/s40145-020-0365-x](https://doi.org/10.1007/s40145-020-0365-x)
31. Kol'chugin AA, Pikalova EYu, Bogdanovich NM, Bronin DI, Filonova EA. Electrochemical properties of doped lanthanum-nickelate-based electrodes. *Russ J Electrochem*. 2017;53(8):826–33. doi:[10.1134/S1023193517080110](https://doi.org/10.1134/S1023193517080110)
32. Wu X, Gu C, Cao J, Miao L, Fu C, Liu W. Investigations on electrochemical performance of La<sub>2</sub>NiO<sub>4+δ</sub> cathode material doped at A site for solid oxide fuel cells. *Mater Res Express*. 2020;7(6):065507. doi:[10.1088/2053-1591/ab9c60](https://doi.org/10.1088/2053-1591/ab9c60)
33. Lenka RK, Patro PK, Patel V, Muhmood L, Mahata T. Comparative investigation on the functional properties of alkaline earth metal (Ca, Ba, Sr) doped Nd<sub>2</sub>NiO<sub>4+δ</sub> oxygen electrode material for SOFC applications. *J Alloys Compd*. 2021;860:158490. doi:[10.1016/j.jallcom.2020.158490](https://doi.org/10.1016/j.jallcom.2020.158490)
34. Skinner SJ, Kilner JA. Oxygen diffusion and surface exchange in La<sub>2-x</sub>Sr<sub>x</sub>NiO<sub>4+δ</sub>. *Solid State Ionics*. 2000;135(1–4):709–12. doi:[10.1016/S0167-2738\(00\)00388-X](https://doi.org/10.1016/S0167-2738(00)00388-X)
35. Sadykov VA, Sadovskaya EM, Pikalova EYu, Kolchugin AA, Filonova EA, Pikalov SM, Ereemeev NF, Ishchenko AV, Lukashevich AI, Bassat JM. Transport features in layered nickelates: Correlation between structure, oxygen diffusion, electrical and electrochemical properties. *Ionics*. 2018;24(4):1181–93. doi:[10.1007/s11581-017-2279-3](https://doi.org/10.1007/s11581-017-2279-3)
36. Zakharchuk K, Kovalevsky A, Yaremchenko A. Characterization of Ruddlesden-Popper La<sub>2-x</sub>Ba<sub>x</sub>NiO<sub>4+δ</sub> nickelates as potential electrocatalysts for solid oxide cells. *Materials*. 2023;16(4):1755. doi:[10.3390/ma16041755](https://doi.org/10.3390/ma16041755)
37. Li Y, Chen G, Chen H-C, Fei L, Xu L, Liu T, Dai J, Huang H, Zhou W, Shao Z. Tailoring the surface cation configuration of Ruddlesden-Popper perovskites for controllable water oxidation performance. *Energy Environ Sci*. 2023;16(8):3331–8. doi:[10.1039/D3EE00380A](https://doi.org/10.1039/D3EE00380A)
38. Zheng Y, Jiang H, Wang S, Qian B, Li Q, Ge L, Chen H. Mn-doped Ruddlesden-Popper oxide La<sub>1.5</sub>Sr<sub>0.5</sub>NiO<sub>4+δ</sub> as a novel air electrode material for solid oxide electrolysis cells. *Ceram Int*. 2021;47(1):1208–17. doi:[10.1016/j.ceramint.2020.08.239](https://doi.org/10.1016/j.ceramint.2020.08.239)
39. Hyodo J, Tominaga K, Ju Y-W, Ida S, Ishihara T. Electrical conductivity and oxygen diffusivity in Cu- and Ga-doped Pr<sub>2</sub>NiO<sub>4</sub>. *Solid State Ionics*. 2014;256:5–10. doi:[10.1016/j.ssi.2013.12.036](https://doi.org/10.1016/j.ssi.2013.12.036)
40. Filonova E, Gilev A, Maksimchuk T, Pikalova N, Zakharchuk K, Pikalov S, Yaremchenko A, Pikalova E. Development of La<sub>1.7</sub>Ca<sub>0.3</sub>Ni<sub>1-y</sub>Cu<sub>y</sub>O<sub>4+δ</sub> materials for oxygen permeation membranes and cathodes for intermediate-temperature solid oxide fuel cells. *Membranes*. 2022;12(12):1222. doi:[10.3390/membranes12121222](https://doi.org/10.3390/membranes12121222)
41. Gilev AR, Kiselev EA, Sukhanov KS, Korona DV, Cherepanov VA. Evaluation of La<sub>2-x</sub>(Ca/Sr)<sub>x</sub>Ni<sub>1-y</sub>Fe<sub>y</sub>O<sub>4+δ</sub> (x = 0.5, 0.6; y = 0.4, 0.5) as cathodes for proton-conducting SOFC based on lanthanum tungstate. *Electrochim Acta*. 2022;421:140479. doi:[10.1016/j.electacta.2022.140479](https://doi.org/10.1016/j.electacta.2022.140479)
42. Wang Z, Miao X, Zhu X, Guo S, Han D, Ye X, Wen Z. Cu, Zn Co-doped ruddlesden-popper La<sub>1.2</sub>Sr<sub>0.8</sub>NiO<sub>4+δ</sub> oxides as high-performance air electrodes of medium-temperature protonic ceramic electrolysis cells. *J Power Sources*. 2024;597:234141. doi:[10.1016/j.jpowsour.2024.234141](https://doi.org/10.1016/j.jpowsour.2024.234141)
43. Solís C, Navarrete L, Serra JM. Study of Pr and Pr and Co doped La<sub>2</sub>NiO<sub>4+δ</sub> as cathodes for La<sub>0.5</sub>WO<sub>11.25-δ</sub> based protonic conducting fuel cells. *J Power Sources*. 2013;240:691–7. doi:[10.1016/j.jpowsour.2013.05.055](https://doi.org/10.1016/j.jpowsour.2013.05.055)
44. Sadykov VA, Sadovskaya EM, Ereemeev NF, Maksimchuk TYU, Pikalov SM, Filonova EA, Pikalova NS, Gilev AR, Pikalova EYu. Structure, oxygen mobility, and electrochemical characteristics of La<sub>1.7</sub>Ca<sub>0.3</sub>Ni<sub>1-x</sub>Cu<sub>x</sub>O<sub>4+δ</sub> materials. *Russ J Electrochem*. 2023;59(1):37–48. doi:[10.1134/S1023193523010068](https://doi.org/10.1134/S1023193523010068)
45. Boehm E, Bassat J-M, Steil MC, Dordor P, Mauvy F, Grenier J-C. Oxygen transport properties of La<sub>2</sub>Ni<sub>1-x</sub>Cu<sub>x</sub>O<sub>4+δ</sub> mixed conducting oxides. *Solid State Sci*. 2003;5(7):973–81. doi:[10.1016/S1293-2558\(03\)00091-8](https://doi.org/10.1016/S1293-2558(03)00091-8)
46. Yashima M, Yamada H, Nuansaeng S, Ishihara T. Role of Ga<sup>3+</sup> and Cu<sup>2+</sup> in the high interstitial oxide-ion diffusivity of Pr<sub>2</sub>NiO<sub>4</sub>-based oxides: Design concept of interstitial ion conductors through the higher-valence d<sup>10</sup> dopant and Jahn-Teller effect. *Chem Mater*. 2012;24(21):4100–13. doi:[10.1021/cm3021287](https://doi.org/10.1021/cm3021287)
47. Maksimchuk T, Filonova E, Mishchenko D, Ereemeev N, Sadovskaya E, Bobrikov I, Fetisov A, Pikalova N, Kolchugin A, Shmakov A, Sadykov V, Pikalova E. High-temperature behavior, oxygen transport properties, and electrochemical performance of Cu-substituted Nd<sub>1.6</sub>Ca<sub>0.4</sub>NiO<sub>4+δ</sub> electrode materials. *Appl Sci*. 2022;12(8):3747. doi:[10.3390/app12083747](https://doi.org/10.3390/app12083747)
48. Kharton VV, Viskup AP, Kovalevsky AV, Naumovich NM, Marques FMB. Ionic transport in oxygen-hyperstoichiometric phases with K<sub>2</sub>NiF<sub>4</sub>-type structure. *Solid State Ionics*. 2001;143(3–4):337–53. doi:[10.1016/S0167-2738\(01\)00876-1](https://doi.org/10.1016/S0167-2738(01)00876-1)
49. Gilev AR, Kiselev EA, Zakharov DM, Cherepanov VA. Effect of calcium and copper/iron co-doping on defect-induced properties of La<sub>2</sub>NiO<sub>4</sub>-based materials. *J Alloys Compd*. 2018;753:491–501. doi:[10.1016/j.jallcom.2018.04.178](https://doi.org/10.1016/j.jallcom.2018.04.178)
50. Tarutin AP, Lyagaeva YG, Vylkov AI, Gorshkov MYU, Vdovin GK, Medvedev DA. Performance of Pr<sub>2</sub>(Ni,Cu)O<sub>4+δ</sub> electrodes in protonic ceramic electrochemical cells with unseparated and separated gas spaces. *J Mater Sci Technol*. 2021;93:157–68. doi:[10.1016/j.jmst.2021.03.056](https://doi.org/10.1016/j.jmst.2021.03.056)

51. Tarutin AP, Lyagaeva JG, Farlenkov AS, Vylkov AI, Medvedev DA. Cu-substituted  $\text{La}_2\text{NiO}_{4+\delta}$  as oxygen electrodes for protonic ceramic electrochemical cells. *Ceram Int*. 2019;45(13):16105–12. doi:[10.1016/j.ceramint.2019.05.127](https://doi.org/10.1016/j.ceramint.2019.05.127)
52. Zhang L, Yao F, Meng J, Zhang W, Wang H, Liu X, Meng H, Zhang H. Oxygen migration and proton diffusivity in transition-metal (Mn, Fe, Co, and Cu) doped Ruddlesden–Popper oxides. *J Mater Chem A*. 2019;7(31):18558–67. doi:[10.1039/C9TA05893A](https://doi.org/10.1039/C9TA05893A)
53. Yashima M, Sirikanda N, Ishihara T. Crystal structure, diffusion path, and oxygen permeability of a  $\text{Pr}_2\text{NiO}_4$ -based mixed conductor ( $\text{Pr}_{0.9}\text{La}_{0.1}$ )<sub>2</sub>( $\text{Ni}_{0.74}\text{Cu}_{0.21}\text{Ga}_{0.05}$ ) $\text{O}_{4+\delta}$ . *J Am Chem Soc*. 2010;132(7):2385–92. doi:[10.1021/ja909820h](https://doi.org/10.1021/ja909820h)
54. Khoshkalam M, Tripković Đ, Tong X, Faghihi-Sani MA, Chen M, Hendriksen PV. Improving oxygen incorporation rate on ( $\text{La}_{0.6}\text{Sr}_{0.4}$ )<sub>0.98</sub> $\text{FeO}_{3-\delta}$  via  $\text{Pr}_2\text{Ni}_{1-x}\text{Cu}_x\text{O}_{4+\delta}$  surface decoration. *J Power Sources*. 2020;457:228035. doi:[10.1016/j.jpowsour.2020.228035](https://doi.org/10.1016/j.jpowsour.2020.228035)
55. Miyoshi S, Furuno T, Sangoanruang O, Matsumoto H, Ishihara T. Mixed conductivity and oxygen permeability of doped  $\text{Pr}_2\text{NiO}_4$ -based oxides. *J Electrochem Soc*. 2007;154(1):B57–62. doi:[10.1149/1.2387103](https://doi.org/10.1149/1.2387103)
56. Filonova EA, Pikalova EYu, Maksimchuk TYu, Vylkov AI, Pikalov SM, Maignan A. Crystal structure and functional properties of  $\text{Nd}_{1.6}\text{Ca}_{0.4}\text{Ni}_{1-y}\text{Cu}_y\text{O}_{4+\delta}$  as prospective cathode materials for intermediate temperature solid oxide fuel cells. *Int J Hydrog Energy*. 2021;46(32):17037–50. doi:[10.1016/j.ijhydene.2020.10.243](https://doi.org/10.1016/j.ijhydene.2020.10.243)
57. Pikalova E, Zhulanova T, Ivanova A, Tarutin A, Fetisov A, Filonova E. Optimized  $\text{Pr}_{1.6}\text{Ca}_{0.4}\text{Ni}_{1-y}\text{Cu}_y\text{O}_{4+\delta}$  phases as promising electrode materials for  $\text{CeO}_2$ - and  $\text{BaCe}(\text{Zr})\text{O}_3$ -based electrochemical cells. *Ceram Int*. 2024;50(20C):40476–91. doi:[10.1016/j.ceramint.2024.06.048](https://doi.org/10.1016/j.ceramint.2024.06.048)
58. Zhulanova T, Filonova E, Ivanova A, Russkikh O, Pikalova E. Control physicochemical and electrochemical properties of  $\text{Pr}_{1.6}\text{Ca}_{0.4}\text{Ni}_{0.6}\text{Cu}_{0.4}\text{O}_{4+\delta}$  as a prospective cathode material for solid oxide cells through the synthesis process. *Solid State Sci*. 2024;156:107671. doi:[10.1016/j.solidstatesciences.2024.107671](https://doi.org/10.1016/j.solidstatesciences.2024.107671)
59. Adler SB. Factors governing oxygen reduction in solid oxide fuel cell cathodes. *Chem Rev*. 2004;104(10):4791–844. doi:[10.1021/cr020724o](https://doi.org/10.1021/cr020724o)
60. Rosten R, Koski M, Koppa E. A guide to the calculation of theoretical densities of crystal structures for solid oxide fuel cells. *J Undergrad Mater Res*. 2006;2(1):38–41. doi:[10.21061/jumr.v2i0.0605](https://doi.org/10.21061/jumr.v2i0.0605)
61. Aguadero A, Alonso J, Escudero M, Daza L. Evaluation of the  $\text{La}_2\text{Ni}_{1-x}\text{Cu}_x\text{O}_{4+\delta}$  system as SOFC cathode material with 8YSZ and LSGM as electrolytes. *Solid State Ionics*. 2008;179(11–12):393–400. doi:[10.1016/j.ssi.2008.01.099](https://doi.org/10.1016/j.ssi.2008.01.099)
62. Sakai M, Wang C, Okiba T, Soga H, Niwa E, Hashimoto T. Thermal analysis of structural phase transition behavior of  $\text{Ln}_2\text{Ni}_{1-x}\text{Cu}_x\text{O}_{4+\delta}$  (Ln = Nd, Pr) under various oxygen partial pressures. *J Therm Anal Calorim*. 2019;135(5):2765–74. doi:[10.1007/s10973-018-7621-0](https://doi.org/10.1007/s10973-018-7621-0)
63. Chen B-H. Introduction of a tolerance factor for the  $\text{Nd}_2\text{CuO}_4(T^-)$ -type structure. *J Solid State Chem*. 1996;125(1):63–6. doi:[10.1006/jssc.1996.0265](https://doi.org/10.1006/jssc.1996.0265)
64. Shannon RD. Revised effective ionic radii and systematic studies of interatomic distances in halides and chalcogenides. *Acta Cryst A*. 1976;32:751–67. doi:[10.1107/S0567739476001551](https://doi.org/10.1107/S0567739476001551)
65. Pikalova E, Kolchugin A, Filonova E, Bogdanovich N, Pikalov S, Ananyev M, Molchanova N, Farlenkov A. Validation of calcium-doped neodymium nickelates as SOFC air electrode materials. *Solid State Ionics*. 2018;319:130–40. doi:[10.1016/j.ssi.2018.02.008](https://doi.org/10.1016/j.ssi.2018.02.008)
66. Choisnet J. Structure and bonding anisotropy in intergrowth oxides: A clue to the manifestation of bidimensionality in  $T^-$ ,  $T'^-$ , and  $T^*$ -type structures. *J Solid State Chem*. 1999;147(1):379–89. doi:[10.1006/jssc.1999.8381](https://doi.org/10.1006/jssc.1999.8381)
67. Nakamura T, Yashiro K, Sato K, Mizusaki J. Oxygen nonstoichiometry and defect equilibrium in  $\text{La}_{2-x}\text{Sr}_x\text{NiO}_{4+\delta}$ . *Solid State Ionics*. 2009;180(4–5):368–76. doi:[10.1016/j.ssi.2009.01.013](https://doi.org/10.1016/j.ssi.2009.01.013)
68. Sadykov VA, Pikalova EYu, Kolchugin AA, Filonova EA, Sadovskaya EM, Ereemeev NF, Ishchenko AV, Fetisov AV, Pikalov SM. Oxygen transport properties of Ca-doped  $\text{Pr}_2\text{NiO}_4$ . *Solid State Ionics*. 2018;317:234–43. doi:[10.1016/j.ssi.2018.01.035](https://doi.org/10.1016/j.ssi.2018.01.035)
69. Kanai H, Mizusaki J, Tagawa H, Hoshiyama S, Hirano K, Fujita K, Tezuka M, Hashimoto T. Defect chemistry of  $\text{La}_{2-x}\text{Sr}_x\text{CuO}_{4-\delta}$ : Oxygen nonstoichiometry and thermodynamic stability. *J Solid State Chem*. 1997;131(1):150–9. doi:[10.1006/jssc.1997.7377](https://doi.org/10.1006/jssc.1997.7377)
70. Naumovich EN, Patrakeev MV, Kharton VV, Yaremchenko AA, Logvinovich DI, Marques FMB. Oxygen nonstoichiometry in  $\text{La}_2\text{Ni}(M)\text{O}_{4+\delta}$  ( $M = \text{Cu}, \text{Co}$ ) under oxidizing conditions. *Solid State Sci*. 2005;7(11):1353–62. doi:[10.1016/j.solidstatesciences.2005.08.005](https://doi.org/10.1016/j.solidstatesciences.2005.08.005)
71. Wang C, Soga H, Okiba T, Niwa E, Hashimoto T. Construction of structural phase diagram of  $\text{Nd}_2\text{Ni}_{1-x}\text{Cu}_x\text{O}_{4+\delta}$  and effect of crystal structure and phase transition on electrical conduction behavior. *Mater Res Bull*. 2019;111:61–9. doi:[10.1016/j.materresbull.2018.10.036](https://doi.org/10.1016/j.materresbull.2018.10.036)
72. Hashimoto T, Yugi T, Sasaki M, Wang C, Sakai M, Soga H, Okiba T. Dependence of crystal structure, morphology and electrical conductivity of  $\text{Pr}_2\text{Ni}_{1-x}\text{Cu}_x\text{O}_{4+\delta}$  and  $\text{PrLaNi}_{1-x}\text{Cu}_x\text{O}_{4+\delta}$  ceramics on Cu content. *ECS Trans*. 2019;91(1):1445–52. doi:[10.1149/09101.1445ecst](https://doi.org/10.1149/09101.1445ecst)
73. Pikalova E, Sadykov V, Sadovskaya E, Ereemeev N, Kolchugin A, Shmakov A, Vinokurov Z, Mishchenko D, Filonova E, Belyaev V. Correlation between structural and transport properties of Ca-doped La nickelates and their electrochemical performance. *Crystals*. 2021;11(3):297. doi:[10.3390/cryst11030297](https://doi.org/10.3390/cryst11030297)
74. Pikalova EYu, Sadykov VA, Filonova EA, Ereemeev NF, Sadovskaya EM, Pikalov SM, Bogdanovich NM, Lyagaeva JG, Kolchugin AA, Vedmid' LB, Ishchenko AV, Goncharov VB. Structure, oxygen transport properties and electrode performance of Ca-substituted  $\text{Nd}_2\text{NiO}_4$ . *Solid State Ionics*. 2019;335:53–60. doi:[10.1016/j.ssi.2019.02.012](https://doi.org/10.1016/j.ssi.2019.02.012)
75. Bamburov A, Naumovich Ye, Khalyavin DD, Yaremchenko AA. Intolerance of the Ruddlesden–Popper  $\text{La}_2\text{NiO}_{4+\delta}$  structure to A-site cation deficiency. *Chem Mater*. 2023;35(19):8145–57. doi:[10.1021/acs.chemmater.3c01594](https://doi.org/10.1021/acs.chemmater.3c01594)
76. Wang Y, Chen J, Liu K, Wang M, Song D, Wong K. Computational screening of  $\text{La}_2\text{NiO}_{4+\delta}$  cathodes with Ni site doping for solid oxide fuel cells. *Inorg Chem*. 2023;62(19):7574–83. doi:[10.1021/acs.inorgchem.3c01044](https://doi.org/10.1021/acs.inorgchem.3c01044)
77. Sadykov VA, Sadovskaya EM, Ereemeev NF, Skriabin PI, Krasnov AV, Bepalko YuN, Pavlova SN, Fedorova YuE, Pikalova EYu, Shlyakhtina AV. Oxygen mobility in the materials for solid oxide fuel cells and catalytic membranes (Review). *Russ J Electrochem*. 2019;55(8):701–18. doi:[10.1134/S1023193519080147](https://doi.org/10.1134/S1023193519080147)
78. Gu X-K, Nikolla E. Design of Ruddlesden–Popper oxides with optimal surface oxygen exchange properties for oxygen reduction and evolution. *ACS Catal*. 2017;7(9):5912–20. doi:[10.1021/acscatal.7b01483](https://doi.org/10.1021/acscatal.7b01483)
79. Tomkiewicz AC, Tamimi MA, Huq A, McIntosh S. The surface oxygen exchange rate linked to bulk ion diffusivity in mixed conducting Ruddlesden–Popper phases? *Faraday Discuss*. 2015;182:13–127. doi:[10.1039/C5FD00014A](https://doi.org/10.1039/C5FD00014A)
80. Huan Y, Chen S, Zeng R, Wei T, Dong D, Hu X, Huang Y. Intrinsic effects of Ruddlesden–Popper-based bifunctional catalysts for high-temperature oxygen reduction and evolution. *Adv Energy Mater*. 2019;9:1901573. doi:[10.1002/aenm.201901573](https://doi.org/10.1002/aenm.201901573)
81. Xue J, Liao Q, Chen W, Bouwmeester HJM, Wang H, Feldhoff A. A new  $\text{CO}_2$ -resistant Ruddlesden–Popper oxide with superior oxygen transport: A-site deficient ( $\text{Pr}_{0.9}\text{La}_{0.1}$ )<sub>1.9</sub>( $\text{Ni}_{0.74}\text{Cu}_{0.21}\text{Ga}_{0.05}$ ) $\text{O}_{4+\delta}$ . *J Mater Chem A*. 2015;3(37):19107–14. doi:[10.1039/C5TA02514A](https://doi.org/10.1039/C5TA02514A)

82. Sadykov VA, Pikalova EYu, Vinokurov ZS, Shmakov AN, Eremeev NF, Sadovskaya EM, Lyagaeva JG, Medvedev DA, Belyaev VD. Tailoring the structural, thermal and transport properties of  $\text{Pr}_2\text{NiO}_{4+\delta}$  through Ca-doping strategy. *Solid State Ionics* 2019;333:30–7. doi:[10.1016/j.ssi.2019.01.014](https://doi.org/10.1016/j.ssi.2019.01.014)
83. Pikalova E, Kolchugin A, Bogdanovich N, Medvedev D, Lyagaeva J, Vedmid' L, Ananyev M, Plaksin S, Farlenkov A. Suitability of  $\text{Pr}_{2-x}\text{Ca}_x\text{NiO}_{4+\delta}$  as cathode materials for electrochemical devices based on oxygen ion and proton conducting solid state electrolytes. *Int J Hydrog Energy*. 2020;45(25):13612–24. doi:[10.1016/j.ijhydene.2018.06.023](https://doi.org/10.1016/j.ijhydene.2018.06.023)